APPLICATION OF THE 2-D CONTINUOUS WAVELET TRANSFORMS FOR CHARACTERIZATION OF GEOLOGICAL AND GEOPHYSICAL DATA

A Dissertation

by

AU KIM VUONG

Submitted to the Office of Graduate and Professional Studies of
Texas A&M University
in partial fulfillment of the requirements for the degree of

DOCTOR OF PHILOSOPHY

Chair of Committee,	Richard L. Gibson
Committee Members,	Akhil Datta-Gupta
	Mark E. Everett
	Yuefeng Sun
	Hongbin Zhang
Head of Department,	Richard Giardino

May 2014

Major Subject: Department of Geology and Geophysics

ABSTRACT

Shatsky Rise, located in the northwest Pacific Ocean, is one of the largest oceanic plateaus. The origin and evolution of the oceanic plateaus are unclear because these features are remote and poorly imaged with geophysical data. Recently, marine multi-channel seismic (MCS) data were collected over Shatsky Rise to image its upper crustal structure. These data have the potential to improve understanding of the processes of basaltic volcanism and the formation and evolution of oceanic plateaus by providing direct insights into the geometry and distribution of igneous eruptions. In contrast to sedimentary settings, it is often difficult to interpret deeper layers within basaltic crust because of rugged layering and scattering. Reflections in igneous crust are characterized by poor lateral continuity compared with marine sediments and often with weak impedance contrasts, resulting in lower signal-to-noise ratio and more challenging interpretation. In this dissertation, we apply the 2-D anisotropic continuous wavelet transform (CWT) method to improve interpretations of MCS data from the Shatsky Rise oceanic plateau. Applying the transform to the time-domain MCS profiles with appropriate values of wavelength and period produces new images with enhanced continuity of reflectors and reduced amplitudes of incoherent noise at different periods. The analysis of the results obtained by using 2-D CWT on the MCS data over the Tamu Massif part of the Shatsky Rise also helps reveal features such as dome-like bulges possibly associated with lava intrusion and faults in the deeper part of the crust associated with volcanic rock. These were not readily seen in the original seismic images, but the suppression of random noise and other signal with low coherence makes their interpretation possible. These and similar results provide new insights into the complexity of the igneous processes

forming Tamu Massif.

The other research topic is to apply the CWT analysis to characterize and measure the roughness of mineral surfaces to understand the effects of geochemical reactions on the surface of the mineral. The effects of the geochemical and environmental reactions process are strongly related to the surface roughness. Because a rough surface has a large number of molecules exposed with unfilled bonds, these molecules have greater energy and react more readily. A thorough knowledge of the surface roughness could lead to better understanding of geochemical reactions and environmental effects on the mineral surface. We apply the 2-D CWT to characterize the surface of two samples of Fe_2O_3 and three samples of calcite. For a fresh surface of the calcite mineral, a cleavage plane exposed by fracturing, the surface measurements show discrete jumps in height because of the limited resolution of measurements. These stair-step-like features have been detected by using 2-D CWT with wavelength of 32.2 μ.

Two other samples of calcite and two samples of Fe_2O_3 show erosion effects and are much rougher. In these cases, the application of 2-D CWT analysis helps to localize the rough features at certain wavelengths of the wavelet, providing better understanding of the characterization of surface roughness. These locations are associated with the high energy surface where we expect the geochemical and weathering reaction initially occur. In the future work, one could implement the 2-D CWT inversion, allowing for the reconstruction of the surface of the mineral at selected wavelengths. Therefore we could observe directly the relationship between the roughness and the wavelength.

DEDICATION

My wife and my two sons Rick, and Stephen.

ACKNOWLEDGEMENTS

I would like to express my appreciation to my advisor Dr. Richard L. Gibson for his guidance, encouragement and support during my study at A&M. I have been learning a lot from him in order to finish this dissertation.

I would like thanks to my committee members, Drs. Hongbin Zhan, Akhil Datta-Gupta, Mark Everett, Benchun Duan, and Yuefeng Sun, for their thorough corrections, questions and advice on my dissertation.

I also thank Dr. William Sager and Dr. Bruce Herbert for their huge contributions to my dissertation.

I thank Saudi Aramco and the U.S. Department of Energy for their research support.

Above all, I would like to thank my wife and two lovely sons Rick and Stephen who have been giving happiness to me.

TABLE OF CONTENTS

Page

LIST OF FIGURES

FIGURE Page

1. INTRODUCTION

1.1 Motivation and overview of research works

In this dissertation, we present two different scientific objectives where we apply the 2-D CWT to study geological and geophysical data. The first one is to characterize the basement of oceanic plateaus of Tamu Massif of Shatsky Rise and the second object is to study the surface roughness of the minerals in order to understand better the effect of geochemical and weathering processes on the surface of the mineral.

1.1.1 The continuous wavelet transform

The wavelet transform (WT) was first introduced by a French geophysicist in 1982 (Morlet et al., 1982). Since then its theoretical formalism as well as its applications have been expanded in many fields such as mechanical engineering, physics, digital signal processing, numerical analysis, geophysics, oceanic and atmosphere science (Foufoula-Georgiou and Kumar, 1994). The localization property in both space (or time) and frequency of WT could extract most of information from non-stationary signal that Fourier transform or even short Window transform can not do. Most of the signal from geological and geophysical data are non-stationary signal, therefore WT is a natural and logical method to apply for these types of data.

The application of WT have been used in the exploration of oil and gas industry as well as in studying earthquake seismic. The application of CWT in seismic imaging have been implemented in several works which are mostly in spectral decomposition detect low frequency shadows beneath hydrocarbon reservoirs (Sun et al., 2003; Sinha et al., 2005), seismic low frequency effects from fluid-saturated reservoirs (Goloshubin et al., 2004; Korneev et al., 2002), and increase the vertical resolution by extending seismic bandwidth (Smith et al., 2008; Kazemeini et al., 2008). In the

recent work (Gersztenkorn, 2012), the 1-D CWT was applied to each trace of the 3-D data in order to have better interpretation of the 3-D seismic profiles. Most of the applications of CWT do not include the normalization factor which is critical to have a quantitative results as discussed in (Torrence and Compo, 1998). Previous seismic applications include studies of earthquake sources parameters (Allmann, 2008); determine uncertainty estimates for wave parameters obtained by seismic-wave radiometry (Poppeliers, 2011), and to characterize the refraction, reflection, coherent noises (Miao and Moon, 1999) and to image the earthquake rupture (Allmann, 2008), and detection of faults (Antoine et al., 2004).

In seismic imaging where the conventional Fourier transform is used, the 2-D seismic data are transformed from space and time domains to wavenumber and frequency, but the results are global in that there is no knowledge of temporal or spatial variations in frequency or wavenumber content. To resolve this issue, the short time Fourier transform was introduced (Allen, 1977) to analyze small sections (time windows) of the signal at particular points in time within signals, however the quality of the results depends on the selection of the window size, which is the same for all frequencies. In contrast, 2-D CWT provide estimates of the local frequency and wavenumber content of the seismic image. The 2-D CWT transform achieves this result by utilizing a localized, 2-D wavelet function instead of the infinite sines and cosines applied in Fourier transforms. The CWT will be used to study the marine seismic data. The scientific problem of the first research topic is to apply the 2-D CWT to characterization of the deeper part of oceanic crust to better understand the volcanism evolution. In this dissertation, we apply the 2-D CWT with a correctly normalized anisotropic Mexican hat wavelet, the first application of this method to seismic image analysis. This normalization, discussed by Torrence and Compo (1998), is important, since our goal is to make quantitative comparisons between sig-

nal content at various frequencies and wavelengths and failure to normalize properly can cause artificial changes in amplitude that are not true measure of variations in signal content.

In material engineering, WT have been used to identify dominant orientations in a porous medium of Massillon sandston (Neupauer and Powell, 2005), and identify the spatial distributions of fractures (Sahimi and Hashemi, 2001). The WT has also been applied to characterize surface of material, such as the 2-D continuous wavelet transform (2-D CWT) have been applied to study the surface roughness to characterize the texture (Josso, 2002), characterization of pitting corrosion to an aluminum alloy (Frantziskonis et al., 2000), the sub-micron surface roughness of anisotropy etched silicon (Moktadir and Sato, 2000), the quality of the painted surface (Mezghania, 2011). For the large surface characterization of the geological data, there have been several works as studying the high resolution topographic data (Booth et al., 2009) for automation landslide mapping and to study the topography of the river bed surface (Nyander et al., 2003). It is still open question since there have been no single method can entirely analyze the surface roughness. In this dissertation, we apply the 2-D CWT for the first time to characterize mineral surface roughness, which has important implications for predicting the effects geochemical and environmental reactions on the mineral surface. The mineral data we use in the dissertation include two samples of Fe_2O_3 and three calcite samples.

1.1.2 Application of the 2-D continuous wavelet transforms to imaging of Shatsky Rise plateau using marine seismic data

The scientific problem of the first research topic is to apply the 2-D CWT to characterization of the deeper part of oceanic crust to better understand the volcanism evolution. Oceanic plateaus are very large igneous provinces in the deep

oceans and are generally a result of massive basaltic volcanism. Observations show that the size of these plateaus ranges up to millions of square kilometers, suggesting they must be explained as a result of the generation of significant volumes of magma in the mantle (Coffin and Eldholm, 1994). Several hypotheses have been proposed to explain the origin of this volcanism, including leaking transform faults (Thomas et al., 1976), spreading ridge reorganization (Anderson et al., 1992), and lithospheric weakening associated with changes in plate stresses (Saunders, 2005). However, these models have difficulty in explaining the large volume of magma in the oceanic plateau. In contrast, the mantle plume head hypothesis (Richards et al., 1989; Mahoney and Spencer, 1991; Coffin and Eldholm, 1994) can explain many features of oceanic plateau, although; there are still some observations that do not fit this hypothesis and may require an alternate explanation (Foulger, 2007). For example, rock recovered from Shatsky Rise shows Mid ocean ridge basalt (MORB) geochemistry and isotopic signatures, in contrast to the plume head model prediction that the plume originates in the lower mantle (Sager, 2005; Mahoney et al., 2005).

Whatever the cause of oceanic plateaus, they are extraordinary volcanoes whose structure and evolution are poorly understood. MCS data can lead to better understanding of the processes of basaltic volcanism and the formation and evolution of oceanic plateaus by giving insights into the geometry of igneous rock layers and other plateau features in the igneous basement. MCS data acquired over ocean plateaus usually provide good images of the upper crustal structure, especially the sedimentary layers. However, it is often difficult to interpret deeper layers, especially those within the igneous basement. That difference in interpretability occurs because sediments typically have continuous, well-layered and easily-traced structural features, whereas volcanic materials are characterized by smaller features with poorer lateral continuity and often with weak impedance contrasts. Since the basement tends to

create weaker reflections, the signal-to-noise ratio decreases, creating additional difficulties that can be exacerbated by the presence of multiples generated by the sea floor and other sources of noise.

We analyzed marine MCS data collected by R/V Marcus G. Langseth across the Tamu Massif of Shatsky Rise in the Northwest Pacific. The seismic data from this experiment display typical problems in imaging basement features. Therefore, we seek to facilitate interpretation by applying 2-D continuous wavelet transforms (CWT) to the data. Conventional applications of Fourier frequency-wavenumber ($f - k$) transforms can help provide insights into data where the signal of interest has a different frequency or wavenumber content from noise. However, a strong limitation arises because the transform is a global approach that measures content of the entire data set, a consequence of the fact that the sinusoidal basis functions applied in the transform are infinite in extent. No measurement of space or time-dependent variation in signal content can be made. In contrast, wavelet transforms utilize a basis function, the wavelet, that is localized in space and time when applied to a time-domain seismic image. It can thus measure variations in frequency and wave-number content as a function of position within the image so that it is possible to identify and extract features of interest more effectively.

Previous seismic applications include studies of earthquake sources (Allmann, 2008) and analysis of data from seismic radiometry (Poppeliers, 2011). Early work applied to seismic reflection data applied the CWT to characterize reflections, refractions and coherent noise in data sets (Miao and Moon, 1999). More recent work has applied the general method to the detection and location of low-frequency "shadows" associated with hydrocarbons (Sun et al., 2003; Sinha et al., 2005), seismic low frequency effects from fluid-saturated reservoirs (Goloshubin et al., 2004; Korneev et al., 2002), earthquake rupture imaging (Allmann, 2008), and detection of faults

(Antoine et al., 2004).

In this study, we apply the 2-D CWT with a correctly normalized anisotropic Mexican hat wavelet, the first application of this method to seismic image analysis. This normalization, discussed by Torrence and Compo (1998), is important, since our goal is to make quantitative comparisons between signal content at various frequencies and wavelengths and failure to normalize properly can cause artificial changes in amplitude that are not true measure of variations in signal content. The results show that application of this CWT help to identify reflecting features in the noisy portion of the images corresponding to igneous basement structures and offer strong potential to improve interpretations.

1.1.3 Multi-scale analysis the surface roughness of the minerals

The second research topic is to apply 2-D CWT to characterize the surface roughness of the minerals to better understand the effect of the geochemical and weathering reaction on the mineral. Characterization surface is an interested research topic in many fields, particularly in material science. The influence of surface morphology on the final paint appearance was studied base on the multi-scale characterization of painted surface (Mezghania, 2011). The surface roughness analysis at different scale was also studied by using discrete wavelet decomposition (Josso, 2002). In material engineering, WT have been used to identify dominant orientations in a porous medium such as the 1 m x 1 m block of Massillon sandstone (Neupauer and Powell, 2005). Environmental effect on structural materials was stied in the paper of Frantziskonis et al., the author showed that using the multi-scale analysis to identify the surface features hidden in digital data of the specimen such as Al 2024-T3 and characterize pitting corrosion to an aluminum alloy. The WT was also used to identify the spatial distributions of fractures (Sahimi and Hashemi, 2001). The char-

acterization surface of material is an open question in industry, 2-D WT are used to characterize the material surface roughness (Moktadir and Sato, 2000; Gaillot et al., 1997). The 2-D CWT was also apply in characterization surface in very large scale such as landslide mapping (Booth et al., 2009), river surface roughness (Nyander et al., 2003).

There has been no single method that can entirely analyze the surface roughness. In this dissertation, the application of 2-D CWT for the first time to apply for characterizing the surface roughness of the mineral to study the effect of the geochemical and environmental reactions on the mineral surface. The minerals that we use in the dissertation are two sample of Fe_2O_3 and three samples of calcite. The topographic maps of the mineral are measured by confocal microscopic. The 2-D CWT can reveal quantitatively the characteristic of the mineral surface. The application of 2-D CWT analysis also help to localize any objects with any size created by geochemical and weathering reactions by carrying out 2-D CWT coefficient at corresponding wavelength. This property help us to understand better the characterization of surface roughness during the geochemical and weathering processes. The 2-D CWT coefficients also help us to localize the positions on the mineral surface with high surface energy. the geochemical and weathering reactions occur initially on these locations.

1.2 Dissertation structure

This section will summarize briefly the content of each chapter. Chapter I gives scientific overview of the dissertation. The two main research topics are presented. The motivation of the research works and the method to approach the existing problems by using CWT are given.

Chapter II is the application of 2-D CWT to characterize the deeper part of the oceanic plateau. The review of the scientific studies of the oceanic plateau are

given at the beginning of the chapter. The existing problem of how to understand better the formation of the oceanic plateau by using marine seismic data are followed. The description of the 2-D marine multiple-chanel seismic (MCS) datas using is this dissertation are given. The chapter includes the geological setting and seismic datas acquired from the Tamu Massif of Shatsky Rise oceanic plateau and the results of 2-D CWT analysis. The review of CWT history as well as its formalism are presented. The synthetic seismic data has been created to show how 2-D CWT work in term of improving the seismic interpretations. The comparison of 2D CWT with $f - k$ is discussed. The results and the discussions of the applicaion of 2D CWT on the two MCS datasets are presented.

Chapter III includes the application of 2-D CWT to study the effect of geochemical reactions on the surface of the minerals. This is for the first time, 2-D CWT is applied to study the small geological data scale. Five mineral datasets used to study are three Calcite minerals and two Fe_2O_3 minerals. The formalism of the surface roughness which is used in building topographic of confocal microscopic have been presented. The topographic maps of these mineral are obtained by confocal microscopic. The description of how the confocal microscopic works has been shown. The topographic maps has been processed to remove spikes before carrying out the surface analysis. The method of removing the spikes is discussed. The surface roughness analysis and discussions of 2D CWT for each mineral have been presented.

Chapter IV review the conclusions of each chapters and summarize the main scientific contributions of the dissertation.

2. APPLICATION OF THE 2-D CONTINUOUS WAVELET TRANSFORMS TO IMAGING OF SHATSKY RISE PLATEAU USING MARINE SEISMIC DATA

2.1 Introduction

Oceanic plateaus are very large igneous provinces (LIPs) in the deep oceans and are generally a result of massive basaltic volcanism. The large size of some of these features suggests they must be explained as a result of the generation of significant volumes of magma in the mantle (Coffin and Eldholm, 1994). Several hypotheses have been proposed to explain the origin of this volcanism, including leaking transform faults (Thomas et al., 1976), decompression melting of fertile mantle at spreading ridge reorganizations (Anderson et al., 1992), and melting caused by lithospheric weakening resulting from changes in plate stresses (Saunders, 2005). However, these alternative models have difficulty in explaining the large volume of magma in the oceanic plateau (Foulger, 2007). In contrast, the mantle plume head hypothesis (Richards et al., 1989; Mahoney and Spencer, 1991; Coffin and Eldholm, 1994) can explain many features of oceanic plateaus, although; there are still some observations that do not fit this hypothesis and may require an alternate explanation (Foulger, 2007). For example, rock recovered from Shatsky Rise shows mid-ocean ridge basalt (MORB) geochemistry and isotopic signatures (Mahoney et al., 2005), rather than lower mantle signatures as is predicted by the plume head model. Recently Sager et al. (2013) proposed that Tamu Massif, the oldest and largest portion of Shatsky Rise, is a single volcano that was formed by a sequence of massive lava fows forming sets of subparallel layers.

Whatever the cause of oceanic plateaus, they are extraordinary volcanoes whose

structure and evolution are poorly understood. MCS data can lead to better understanding of the processes of basaltic volcanism and the formation and evolution of oceanic plateaus by giving insights into the geometry of igneous rock layers and other plateau features in the igneous basement. MCS data acquired over ocean plateaus usually provide good images of the upper crustal structure, especially the sedimentary layers. However, it is often difficult to interpret deeper layers, especially those within the igneous basement. That difference in interpretability occurs because sediments typically have continuous, well-defined, and easily-traced layers, whereas volcanic materials are characterized by less regular features with poorer lateral continuity and often with weak impedance contrasts. Because layers within the basement tend to create weaker reflections, the signal-to-noise ratio decreases, creating additional difficulties that can be exacerbated by the presence of multiples generated by the sea floor and other sources of noise.

We analyzed marine MCS data collected by *R/V Marcus G. Langseth* across the Tamu Massif of Shatsky Rise. These data display typical problems in imaging basement features. Therefore, we seek to facilitate interpretation by applying 2-D continuous wavelet transforms (CWT) to the data. Conventional applications of Fourier frequency-wavenumber ($f - k$) transforms can help provide insights into data where the signal of interest has a different frequency or wavenumber content from noise. However, a strong limitation arises because the transform is a global approach that measures the content of the entire data set, a consequence of the fact that the sinusoidal basis functions applied in the transform are infinite in extent. No measurement of space or time-dependent variation in signal content can be made. In contrast, wavelet transforms utilize a basis function, the wavelet, that is localized in space and time when applied to a time-domain seismic image. It can thus measure variations in frequency and wave-number content as a function of position

within the image so that it is possible to identify and extract features of interest more effectively. Previous seismic applications include studies of earthquake sources (Allmann, 2008) and analysis of data from seismic radiometry (Poppeliers, 2011). Early work applied to seismic reflection data applied the CWT to characterize reflections, refractions and coherent noise in data sets (Miao and Moon, 1999). More recent work has applied the general method to the detection and location of low-frequency "shadows" associated with hydrocarbons (Sun et al., 2003; Sinha et al., 2005), seismic low frequency effects from fluid-saturated reservoirs (Goloshubin et al., 2004; Korneev et al., 2002), earthquake rupture imaging (Allmann, 2008), and detection of faults (Antoine et al., 2004). In this study, we apply the 2-D CWT with a normalized anisotropic Mexican hat wavelet (Antoine et al., 2004). The wavelet normalization, the first application of this method to seismic image analysis. This normalization, discussed by Torrence and Compo (1998), is important, since our goal is to make quantitative comparisons between signal content at various frequencies and wavelengths and failure to normalize properly can cause artificial changes in amplitude that are not true measure of variations in signal content. To the best of our knowledge, this normalization has not previously been applied for geophysical interpretation applications. The results show that application of this CWT help to identify reflecting features in the noisy portion of the images corresponding to igneous basement structures and offer strong potential to improve interpretations. An important motivation for testing its utility on the Shatsky Rise seismic data is to help verify the hypothesis of Sager et al. (2013) that suggests the Tamu Massif is a single volcano comprised of subparallel lava flows. If the CWT approach is useful, it will facilitate more detailed interpretations of structure in the igneous basement that will either be consistent with this hypothesis or contradict it.

The chapter is organized as follows. We first briefly review the geologic setting

of the Shatsky Rise and important problems associated with explaining the origin and development of such plateaus. In this context, we comment on previous seismic imaging studies of the plateau and summarize some general characteristics of the seismic data that we utilize in this work. Example data sections from the Tamu Massif show some obvious reflecting structures but also have serious problems with noise in the deeper portions of the geologic section. We then summarize the formalism of the 1-D and 2-D CWT to illustrate its application and provide examples to show both how it can help clarify noisy seismic images and how to interpret results. The results of the 2-D CWT using the Mexican hat wavelet on synthetic test data show clearly that we can characterize important features of the synthetic data by choosing appropriate parameters. Finally we present the analysis of the 2-D CWT results from the field data and give some summary interpretations, noting some new geologic features suggested by the CWT images that had previously been identified. These structures suggest additional complexity in the processes forming Tamu Massif than those previously proposed by Sager et al. (2013).

2.2 Shatsky Rise: geologic setting and seismic data

The Shatsky Rise oceanic plateau is located ∼1600 km east of Japan in the northwest Pacific Ocean (Figure 2.1). It has dimensions of 1650 km by 450 km and the depth ranges from about 2.0 km to 5.5 - 6.0 km, the depth of the surrounding seafloor. Three large volcanic edifices are defined in the Shatsky Rise, namely the Tamu, Ori, and Shirshov massifs and a low ridge, the Papanin Ridge, extends from the north of the plateau (Sager et al., 1999) (Figure 2.1). In addition, a low ridge, the Papanin Ridge, extends from the north of the plateau (Sager et al., 1999). The Tamu Massif is the oldest and largest of the volcanic structures (Mahoney et al., 2005; Sager, 2005).

The Shatsky Rise began to form at about the time of magnetic anomalies M21 and M20, which have ages of 149 Ma and 147 Ma, respectively (Gradstein et al., 2004). Although the Tamu Massif may have formed rapidly (Sager and Han, 1993), the total duration of volcanic activity forming Shatsky Rise was about 21 million years (Nakanishi et al., 1999). Volcanic basement has subsequently been covered by sediments that are generally thin on the flanks but can be as much as ∼1 km thick at the summit (Houtz and Ludwig, 1979; Ludwig and Houtz, 1979; Sliter and Brown, 1993). Igneous cores have been obtained from six drill sites on Shatsky Rise, Site 1213 on Ocean Drilling Program (ODP) Leg 198 (Shipboard Scientific Party, 2002; Bralower et al., 2006) and five sites during Integrated Ocean Drilling program (IODP) Expedition 324 (Sager et al., 2010) (Figure 2.1). Two types of basaltic lava flows were recovered at most of the drill sites, pillow lavas with thicknesses on the order of 0.2 m to 1.0 m, and massive flows up to ∼23 m in thickness (Sano et al., 2012). The massive flows dominate at the Tamu massif (Sager et al., 2011; Sager et al., 2012). According to recent seismic refraction results, the maximum crustal thickness of the plateau is ∼30 km, showing that the Shatsky Rise plateau was formed from a very large volume of magma (Korenaga and Sager, 2012). Several potential explanations have been proposed for the formation of this plateau (Thomas et al., 1976; Anderson et al., 1992; Coffin and Eldholm, 1994). The plume head model (Coffin and Eldholm, 1994) suggests that the oceanic plateau formed by the ascent of a large plume from the lower mantle to the oceanic lithosphere, where it erupted to form Shatsky Rise. Many of observations from Shatsky Rise are consistent with the plume head hypothesis (Nakanishi et al., 1999; Sager, 2005), but there are some aspects that do not fit. For example, geochemical and isotopic studies of basalt samples from the plateau give results that are similar to MORB rather than lower mantle sources as would be expected from the mantle plume (Mahoney et al., 2005).

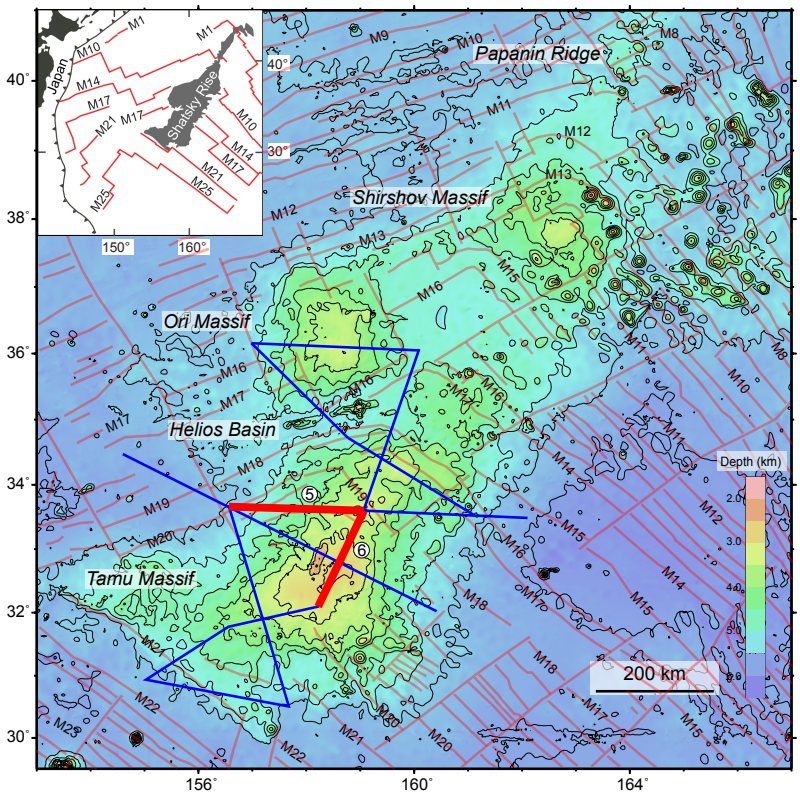

Figure 2.1: MCS lines over Shatsky Rise. In this paper we consider seismic Lines 5 and 6 (heavy red lines). Bathymetry is from satellite-predicted depths with 500-m contours (Smith and Sandwell, 1997). The light red lines show magnetic lineations with chron numbers labeled for reference (Nakanishi et al., 1999). Heavy blue lines show MCS reflection profiles collected by *R/V Marcus G. Langseth*. Inset depicts the location of Shatsky Rise relative to Japan and nearby subduction zones (toothed lines) and the wider magnetic pattern.

This provides strong incentive for additional studies of the plateau to obtain new and better constraints on its geometry, composition and structure to determine if these aspects of the Shatsky Rise are consistent with the mantle plume hypothesis. Detailed seismic images have the potential to provide important insights into the geometry of igneous rock structures for this purpose. In addition, the seismic data can help understand lateral variations in structures and materials found in the core samples taken at the relatively sparse drill sites.

2.2.1 2-D marine multi-channel seismic data

Older marine seismic data collected over the Shatsky Rise are low resolution, analog, single-channel seismic profiles, which limited in resolution and penetration. Such profiles typically show the thickness of the sediments and gross sedimentary layering, but little detail within the igneous crust. Low-fold, digital, MCS profiles were acquired in 1994 (Sager et al., 1999; Klaus and Sager, 2002). Because the seismic source was relatively low in strength, the seismic data show only weak amplitude signals in the volcanic basement (Sager et al., 1999). Two recent cruises acquired new seismic lines utilizing the *R/V Marcus G. Langseth* with a 6660 cubic-inch (108.2 L) air gun array source and 5.85-km-long, 468 channel seismic streamer in an attempt to image the volcanic basement more clearly (Zhang et al.). The locations of these MCS data lines are shown in Figure 2.1. We analyze portions of two of these new MCS profiles, Lines 5 and 6 (Figure 2.1; Zhang et al.). The former crosses the summit of Tamu Massif from southwest to northeast, whereas the latter runs east-west down the western slope from the axis of the massif to near the base. These MCS data were processed using the ProMAX software system with a standard work flow including the following general steps: geometry setup, trace edit, bandpass filter, deconvolution, velocity analysis, normal move-out, stack, time migration (Zhang et al.). Parts of seismic profiles for Lines 5 and 6 are shown in Figures 2.2 and 2.3. The post-process time and space sample intervals are 4 ms and 6.25 m, respectively, for the seismic images.

2.3 Continuous wavelet transforms

The wavelet transform (WT) was first introduced by a French geophysicist in 1982 (Morlet et al., 1982). Since then it has been developed in the theoretical formalism as well as applications in many fields such as mechanical engineering, physics, digital

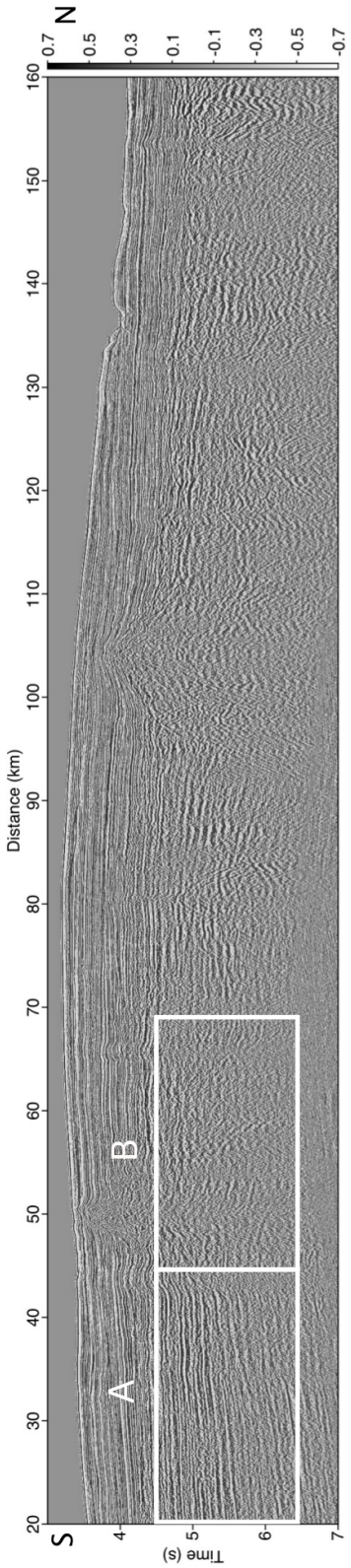

Figure 2.2: MCS data Line 6. The location of this line is shown in Figure 2.1. The white boxes show the seismic data we used for 2-D CWT calculation.

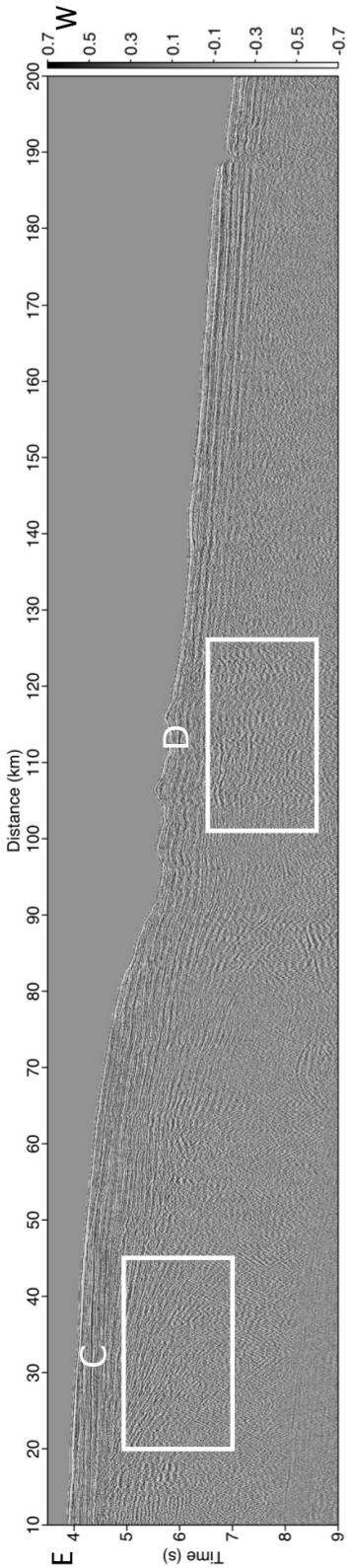

Figure 2.3: MCS data Line 5. The location of this line is shown in Figure 2.1. The white boxes show the seismic data we used for 2-D CWT calculation.

signal processing, numerical analysis, geophysics, oceanic and atmosphere science (Foufoula-Georgiou and Kumar, 1994). The localization property in both space (or time) and frequency of WT could extract most of information from non-stationary signal that Fourier transform or even short Window transform can not do. Most of the signal from geological and geophysical data are non-stationary signal, therefore WT is a natural and logical method to apply for these types of data.

In seismic imaging where the conventional Fourier transform is used, the 2-D seismic data are transformed from space and time domains to wavenumber and frequency, but the results are global in that there is no knowledge of temporal or spatial variations in frequency or wavenumber content. To resolve this issue, the short time Fourier transform was introduced (Allen, 1977) to analyze small sections (time windows) of the signal at particular points in time within signals, however the quality of the results depends on the selection of the window size, which is the same for all frequencies. In contrast, 2-D CWT provide estimates of the local frequency and wavenumber content of the seismic image. The 2-D CWT transform achieves this result by utilizing a localized, 2-D wavelet function instead of the infinite sines and cosines applied in Fourier transforms. The CWT will be used to study the marine seismic data.

In seismic data analysis where the conventional Fourier transform is used, 2-D seismic data are transformed from space and time domains to wavenumber and frequency, but the results are global in that there is no knowledge of temporal or spatial variations in frequency or wavenumber content. To resolve this issue for spectral analysis, the short time Fourier transform was introduced to analyze small sections (time windows) of the signal at particular points in time (Allen, 1977). However, the quality of the results depends on the selection of the window size, which is the same for all frequencies. The wavelet transform (WT) was developed

to address these problems (Morlet et al., 1982). Since its introduction, a number of advances have been made both in the theoretical foundations and applications of the WTs in many fields such as mechanical engineering, physics, digital signal processing, numerical analysis, geophysics, oceanic and atmospheric science (Foufoula-Georgiou and Kumar, 1994).

Although all applications in this paper apply a 2-D wavelet transform, we begin by presenting the 1-D form to illustrate the basic idea and key expressions. The CWT is the convolution of the signal $f(x)$ with basis functions $\psi_{s,a}(x)$. These basis functions are generated from a mother function $\psi(x)$ by applying translation a and dilation s:

$$\psi_{s,a}(x) = \frac{1}{\sqrt{s}}\psi\left(\frac{x-a}{s}\right). \tag{2.1}$$

A number of wavelet functions have been proposed, and in our work we utilize the Mexican hat wavelet function, which in 1-D is (Addison, 2002)

$$\psi(x) = \frac{2}{\sqrt{3}\pi^{-1/4}}\left(1-x^2\right)e^{-x^2/2}. \tag{2.2}$$

The general expression for the wavelet transform of the signal $f(x)$ is (Daubechies, 1992)

$$C(s,a) = \int_{-\infty}^{\infty} f(x)\psi^*\left(\frac{x-a}{s}\right)dx, \tag{2.3}$$

where $*$ represents the complex conjugate operation. The translation a applies the transform to different times or positions in the data, and the dilation s corresponds to the scale, which is analogous to period. The CWT coefficients measure in essence the similarity of the signal $f(x)$ with the wavelet at a particular scale. Thus the high frequency features of the signal are better detected at small scales, and the low frequency features can be better characterized at long scales. In the case of the

Mexican hat wavelet, the relationship between scale s and the wavelet period T is given by (Torrence and Compo, 1998)

$$T = \frac{2\pi}{\sqrt{5/2}} s. \tag{2.4}$$

If the primary task is to measure variations in frequency content with time in seismic data, this 1-D transform would suffice. However, for analysis of 2-D seismic images, we apply the 2-D anisotropic Mexican hat wavelet described by the following equation (Antoine et al., 2004):

$$\psi_{s,a,b}(x, y, \sigma) = \frac{1}{s\sqrt{K_\psi}} \left(2 - \frac{(x-a)^2}{s^2\sigma^2} - \frac{(y-b)^2}{s^2} \right) e^{-\frac{1}{2}\left(\frac{(x-a)^2}{s^2\sigma^2} + \frac{(y-b)^2}{s^2} \right)} \tag{2.5}$$

where a and b are the translation parameters in the x and y directions, respectively. For application to seismic images, the variables x and y will normally correspond to the horizontal and vertical directions, respectively, or distance and two-way time. The parameter σ is the aspect ratio, or the ratio between the widths of the wavelet measured in the vertical and horizontal directions, and it measures the anisotropy of the wavelet. This anisotropy will be important for application to time-domain migration images where these two directions correspond to two-way reflection time and distance. The two scales $s\sigma$ and s are chosen independently to measure signal content at the wavelength and period, respectively, of interest (the wavenumber and frequency are given by the reciprocals of these values).

The normalization constant K_ψ in equation 2.5 is defined assuming $s = 1$ and can be expressed with $a = b = 0$ since it is independent of position (Gaillot et al.,

1997; Darrozes et al., 1997):

$$K_\psi = (2\pi)^2 \int_{-\infty}^{\infty}\int_{-\infty}^{\infty} \frac{|\psi_{s,a,b}(x,y,\sigma)|^2}{x^2+y^2} dxdy = \frac{\sigma^2}{16\pi^3}. \tag{2.6}$$

The influence of scale on the normalization is included through the quantity $1/s$ in equation 2.5. If the aspect ratio parameter in this wavelet is large, the wavelet is wide compared to its height, which would be appropriate for a horizontal reflector in a seismic image, since reflections from interfaces typically extend over many traces laterally, but over a comparatively small number of time units in the vertical dimension in the image. However, in some cases as reflector may have a comparatively large dip angle. In this case, the wavelet can be rotated about an angle θ prior to calculations, and the transform can also be used in general to assess dipping signal content as well as variations in frequency and wavenumber. The rotation operator R_θ is applied to rotate coordinates at the point of interest before applying the translation and scale parameters utilizing a standard rotation matrix multiplied by a data vector (x, y) in the form

$$R_\theta(x,y) = \begin{bmatrix} cos\theta & -sin\theta \\ sin\theta & cos\theta \end{bmatrix} \begin{bmatrix} x \\ y \end{bmatrix}, \tag{2.7}$$

thereby allowing the wavelet transform to help identify features of different orientations as well as shapes and sizes. Figure 2.4 shows an example of the Mexican hat wavelet with $\theta = 45°$. Because the structure of an oceanic plateau is generally relatively flat, most of our calculations in our investigation utilized a rotation angle of $\theta = 0$. The 2-D continuous wavelet transform is the 2-D convolution of the data $f(x, y)$ and the wavelet function and the expression is directly comparable to that in

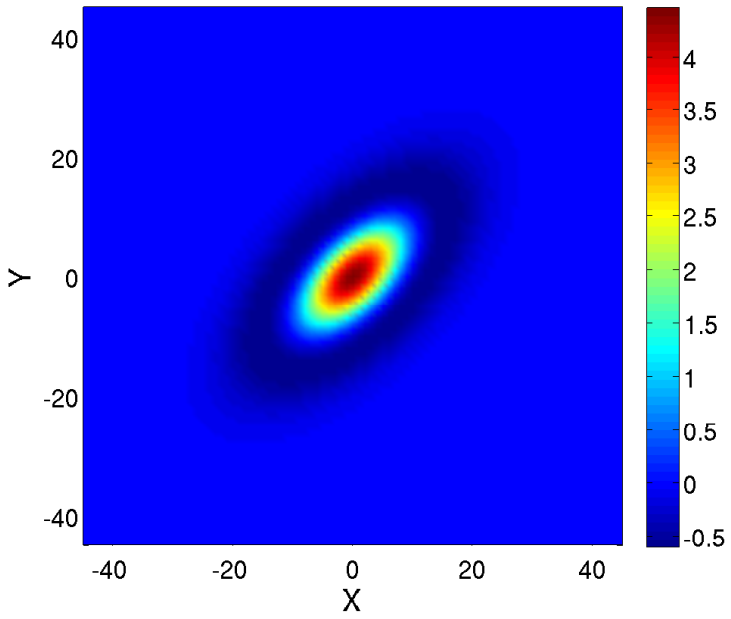

Figure 2.4: 2-D normalized anisotropic Mexican hat wavelet (equation 2.5) with aspect ratio $\sigma = 2$, rotation angle $\theta = 45$, and scale $s = 5$ (equation 2.4).

equation 2.3,

$$C(s, a, b, \sigma, \theta) = \int_{-\infty}^{\infty} \int_{-\infty}^{\infty} f(x, y) \psi^* \left[R_\theta \left(\frac{x/\sigma - a}{s}, \frac{y - b}{s} \right) \right] dxdy, \tag{2.8}$$

where a and b are the two translation parameters and s is again dilation. The 2-D CWT coefficients can determine the match between the signal and the wavelet at scales of interest. A large coefficient $C(s, a, b, \sigma, \theta)$ results when the wavelet in the convolution integral in equation 2.8 has a frequency and wavelength scales comparable to features in the data at the location given by $(x, y) = (a, b)$. Displaying coefficient values as a function of distance and time in a seismic migration image will give quantitative measures of the variation in frequency and wavenumber of reflectors in the image. Using a correct normalization, division by $s\sqrt{K_\psi}$, is essential

to gain quantitative measures of signal content at different wavelengths and periods (Torrence and Compo, 1998), but to our knowledge previous applications to seismic imaging neglect this term.

2.3.1 Tests on 2-D synthetic seismic images

Application of the CWT to a simple 2-D synthetic data set provides insights that show how to interpret results and helps to illustrate its potential to improve image interpretation when signal-to-noise ratio is low. The synthetic seismic section was created by convolving a series of reflection coefficients, corresponding to three groups of reflectors of varying width, with a Ricker wavelet. In addition, random noise was added to the image with a signal-to-noise ratio of 0.75 (Figure 2.5A).

The presence of this strong noise partially obscures the reflection signals and their terminations within the image. Test horizontal reflectors have lengths of 62.5 m, 187.5 m and 437.5 m, and two shallow and two deep reflectors applied frequencies of 31 and 10 Hz, respectively. The combination of different sizes and frequencies in CWT show how CWT coefficients are able to measure such variability in field data. Discretization intervals in time and space were set to 4 ms and 6.25 m. We will show that by using 2-D CWT with a 2-D anisotropic Mexican hat wavelet, we can detect the test targets at different horizontal wavelengths of the wavelet and also illustrate the influence of the wavelet frequency on the vertical resolution of the seismic data. In this synthetic test, we computed CWT coefficients (equation 2.8) with frequencies of 10 Hz and 31 Hz, setting the rotation angle to zero because the reflectors are horizontal.

CWT coefficient results from the synthetic model for 10 Hz show several important properties of the transform comparing horizontal wavelengths of 187, 437 and 800 m (Figure 2.5; Note: because the transform computes a value at each pair of

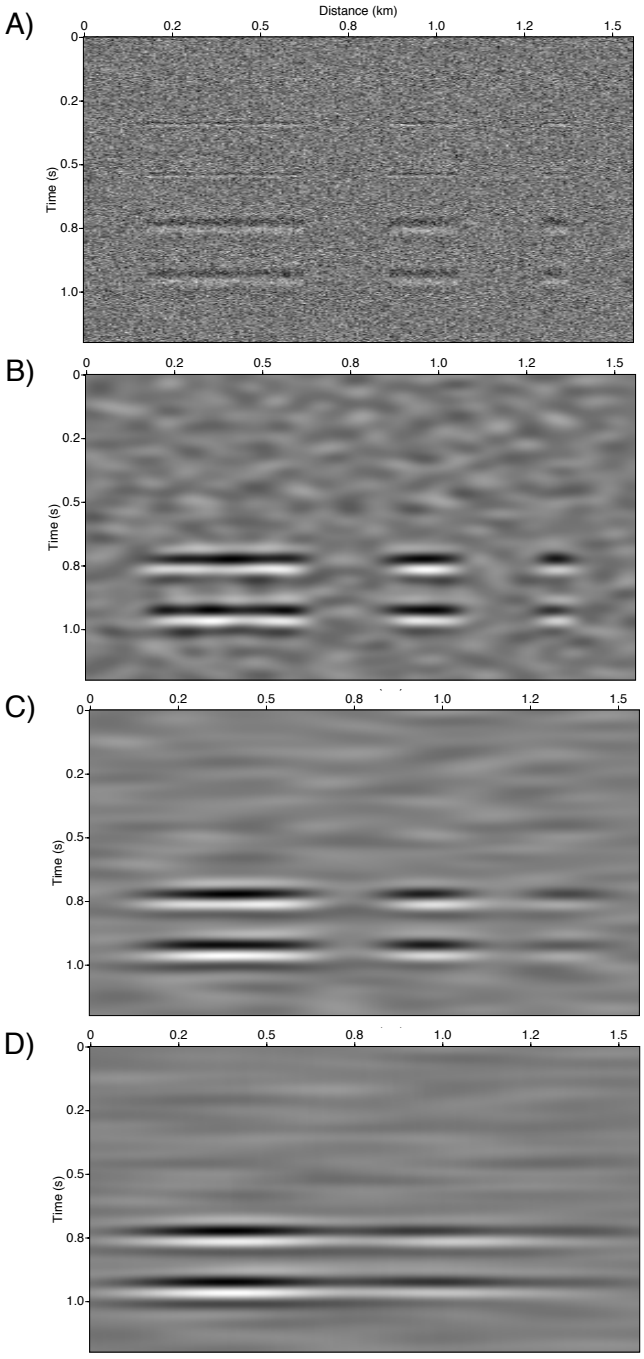

Figure 2.5: (A) Test 2-D synthetic seismic section with random noise (signal-to-noise ratio 0.75). The shallow reflectors have Ricker wavelets with frequency 31 Hz, while the deeper versions have frequency 10 Hz. The lower three panels are CWT coefficient sections at frequency 10 Hz with wavelengths (B) 187 m, (C) 437 m and (D) 800 m.

distance and time coordinates, these coefficients are analogous to seismic traces and are plotted as such in this and subsequent figures). A clear dependence on frequency is observed, with increased signal to noise at greater wavelengths countered by reduced horizontal resolution. Since the noise is uncorrelated horizontally from trace to trace in the image, noise influence on coefficients decreases rapidly with increasing wavelength. Thus coefficients at long wavelengths show the greatest reduction in noise amplitude with respect to signal strength. At the same time, small features are smeared horizontally at at long wavelengths, and the coefficients fail to clearly distinguish the three separate reflectors for a wavelength value of 800 m (Figure 2.5D). Although the coefficient magnitude does decrease subtly between the real reflector positions for the long wavelength solution, it is easier to detect the gaps present between targets at the shorter wavelengths. Even for the shortest wavelength, the reflectors are easier to identify than in the raw data, because the noise has minimal influence on the computed coefficients (Figure 2.5B). Noise with spatial or temporal correlation will not be suppressed as effectively, but incoherent noise in field data images arising from processing artifacts or other uncorrelated sources should be minimized.

Comparing these lower frequency coefficients to values for 31 Hz shows that many of the same observations apply (Figure 2.6). The transform makes it easier to find reflectors at long wavelength values, for all features in the test image. The long wavelength coefficients will still lead to some horizontal smearing, but this effect is not as significant at the higher frequency. Also, it is clear that the improved resolution with the higher frequency wavelet allows easier identification of the truncations of the separate target reflectors. The primary limitation of these results is that it is hard to see the high frequency targets with the smallest width. Although the coefficient plots at long wavelength are influenced primarily by the signal in the presence of

uncorrelated noise, the reflectors themselves, with width 62.5 m, are much smaller than the wavelet wavelength and do not create large wavelet coefficients: the CWT coefficients are sensitive to both the temporal frequency and the spatial wavelength of the signal content.

These CWT results suggest several guidelines for interpreting results from field data. First, the transform should clarify coherent features in images affected by relatively incoherent noise because the CWT coefficients are large when the signal includes coherent signal associated with geologic structure. The coefficient displays can also help assess size scales of features, but if the wavelet wavelength is too long, especially at lower frequencies, lateral resolution will be diminished. In general, high frequencies should be preferred, since time and spatial resolution are better. However, signal is generally weaker at high frequencies, especially for deep crustal targets, which will likely restrict application to low frequencies for field data.

2.3.2 Comparison to bandpass filters

Comparisons of these CWT coefficient results with conventional bandpass filtering helps illustrate the differences in the operation of the wavelet approach (Figure 2.7). Since the synthetic reflection signals have frequencies of 10 and 30 Hz, we filtered the data with bandpass filters centered on those two values. The corner frequencies for the zero-phase filter were 3, 8, 12 and 20 Hz for the low frequency case and 12, 20, 40 and 55 Hz for the filter designed to enhance the 30 Hz reflectors. The filters applied sine-squared tapers. While this filtering does make the reflectors slightly more visible than compared to the original, noisy synthetic, the signal-to-noise ratio in the surrounding portions of the image is still much lower than for the CWT. This is not surprising, since the CWT coefficients also apply a finite horizontal wavelength. The random noise is uncorrelated from trace-to-trace, and therefore as wavelength

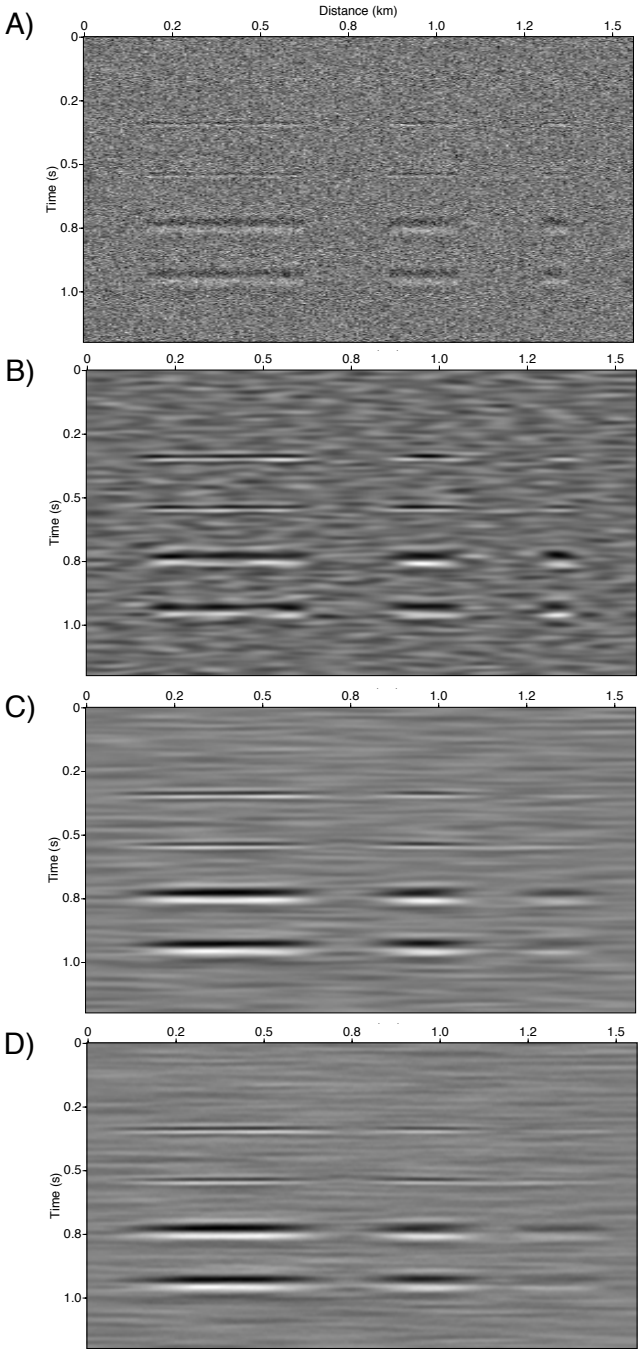

Figure 2.6: (A) Test 2-D synthetic seismic section with random noise (signal-to-noise ratio 0.75). The lower three panels are the 2-D CWT coefficient sections for frequency 31 Hz and several wavelengths: (B) 187 m, (C) 437 m, and (D) 800 m.

increases, the signal-to-noise ratio of the images increases. Uncorrelated noise has negligible contribution to coefficients for the finite wavelengths. It is reasonable to think of the CWT results as a filtering operation to extract signal content at desired spatial and temporal scales (Torrence and Compo, 1998). Therefore, the CWT approach will be beneficial when the image contains noise at different spatial and frequency scales than the signal. If the noise has not particular spatial scale, and is primarily present at specific frequencies, bandpass filtering may suffice. In principle, $f - k$ filtering might help to increase signal-to-noise ratio somewhat more compared to simple band-pass filters, but it is very difficult to implement reliably for the field data which include reflectors with large ranges of dips without suppressing desired signal.

2.4 2-D CWT results

The complete seismic profiles in Figures 2.2 and 2.3 are too large to apply the CWT along their entire lengths and to display and visualize the results effectively. For this reason, we selected portions of these seismic profiles that include both simple and more complicated geological structures to demonstrate the results of the CWT and to discuss implications for interpretation of geologic structures. We carried out the CWT calculations for the areas marked with the white boxes in Figures 2.2 and 2.3. Assuming a seismic velocity of 4000 m/s for the igneous basement (Zhang et al., in this dissertation), the boxes on Line 6 correspond to depths ranging from near the top of the igneous basement to about 4000 m below. For Line 5, the two areas correspond to depths about 1000 m to 5000 m below the top of the igneous basement. Given these subsets of the data, we can test the utility of CWT results at various spatial and temporal scales to extract features of interest, such as those that might be related to volcanic intrusions and associated features deep

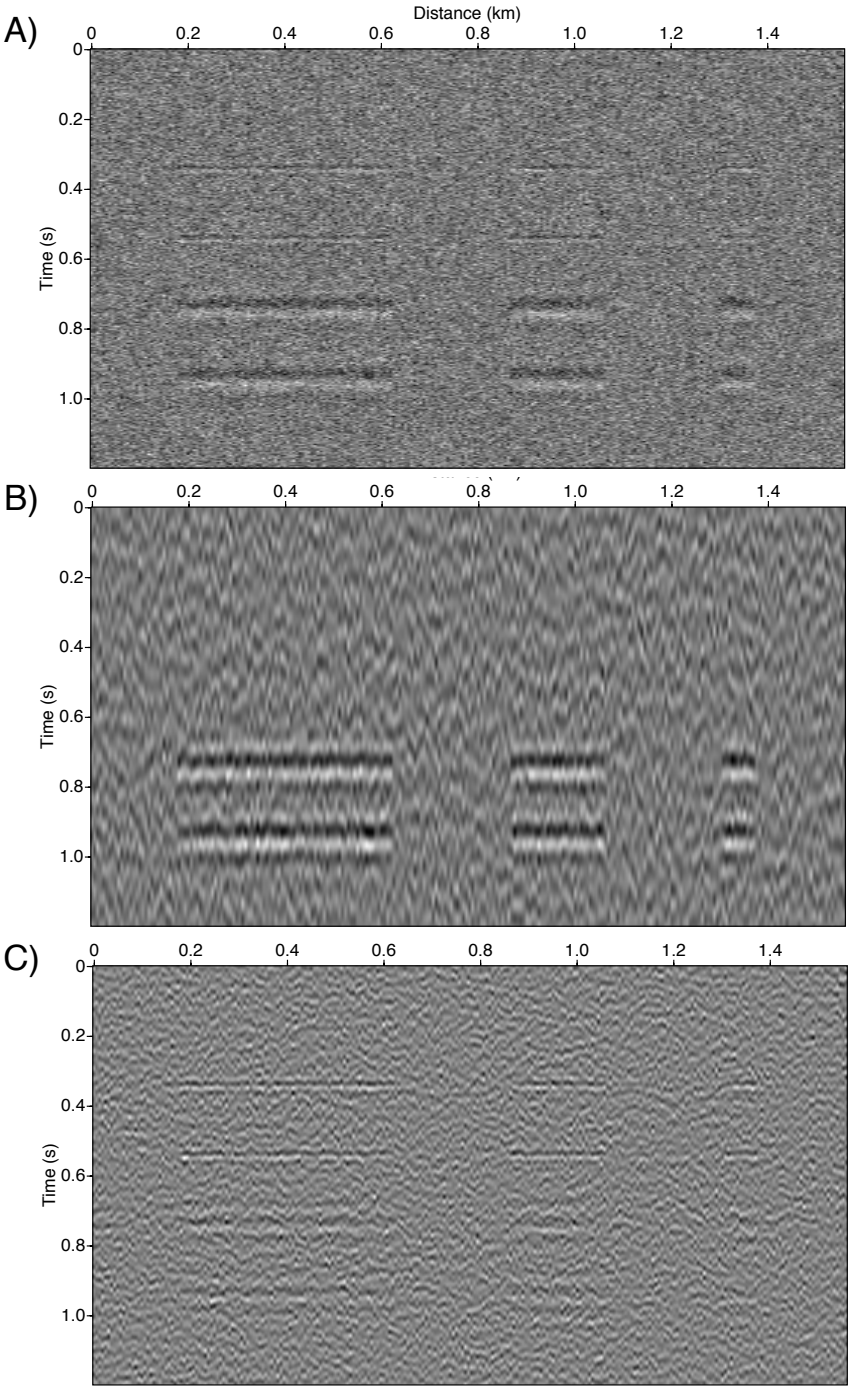

Figure 2.7: Comparison of (A) test 2-D synthetic seismic section with random noise (signal-to-noise ratio 0.75), (B) result of a bandpass filter centered on 10 Hz, and (C) a bandpass filter centered on 30 Hz. Details of filter design are provided in the text.

in the crust within the Tamu Massif. While the general CWT formulation allows for analysis of dipping features, most of the reflectors are nearly horizontal, and we therefore first set the rotation angle to zero (equation 2.8). The aspect ratio constant σ is chosen in order to compute wavelet coefficients at horizontal length scales ranging from 50 m to 3000 m to design transforms assisting in interpretation tasks. Measurements of the frequency spectra of these seismic sections suggest that the strongest frequency content is around 30 Hz. Because attenuation limits signal content at higher frequencies, we present CWT results for frequencies near 30 Hz and 10 Hz.

In the following sections, we will first present results for Line 6, where reflectors can be inferred visually from the somewhat noisy data, before proceeding to the more challenging case of Line 5, which is much more challenging to interpret. Though the improvements are more useful for applications in the latter case, we begin with Line 6 to build on the insights of the synthetic data test case (Figs. 2.5, 2.6) to help show how the CWT results provide improvements first in a case where the signal is not too hard to identify. In addition, we will present results for a range of frequencies and horizontal wavelengths. Not all of these results are directly useful for interpretation, but comparing results for different values helps to clarify and support choices in later examples. This initial set of results for the field data makes it easier to understand what the CWT coefficients are measuring. Given the results to help demonstrate that the CWT approach does truly provide reliable insights into the data structure in the seismic images, we conclude with examples from Line 5 where the reflection signal-to-noise ratio is much lower.

2.4.1 CWT applied to line 6

The total length of Line 6 is about 197 km, but our analysis concentrates on two areas marked with the white boxes in Figure 2.2, each about 25 km long, for application of the CWT. The first, Box A near the beginning of the seismic profile in Figure 2.2, is a section which extends from 20 km to 45 km (Figure 2.8A), where we can see reflectors interpreted as lava flows that emanated from the volcanic center and flowed down the flank to the left in the image (Zhang et al.). While some reflectors are clear and continuous in the section between two-way times of 4.5 and about 5.5 s, deeper features are less continuous and difficult to follow. The seismic profile also shows that the image has decreased signal strength in the area from 43 km to 45 km with two-way travel time from 4.5 s to 6.5 s. Another section extends from 45 km to 70 km, where we can see many intra-basement reflectors.

Figure 2.8B displays the 2-D CWT result at a frequency of 10.5 Hz and horizontal wavelength of 149 m. Because this frequency is lower than much of the signal, which includes significant content at frequencies over 30 Hz, reflectors in the image have lower frequency content and are broader in time. It is nonetheless easier to identify some laterally continuous events than in the original image. For example, there are a number of continuous lateral events from 4.5 s to 5.7 s. We can see that this CWT coefficient is not strongly affected by the high frequency and high wavenumber noise that is hindering identification of reflections in the original data image. Increasing the wavelength parameter to 3 km (Figure 2.8) does provide an image with more continuous reflectors, but this should be compared to the synthetic test (Figure 2.5), where long wavelengths have much reduced horizontal resolution. This wavelength of 3 km is therefore not an effective choice for interpretation of this data section.

These CWT coefficients are compared to analogous results at a frequency of

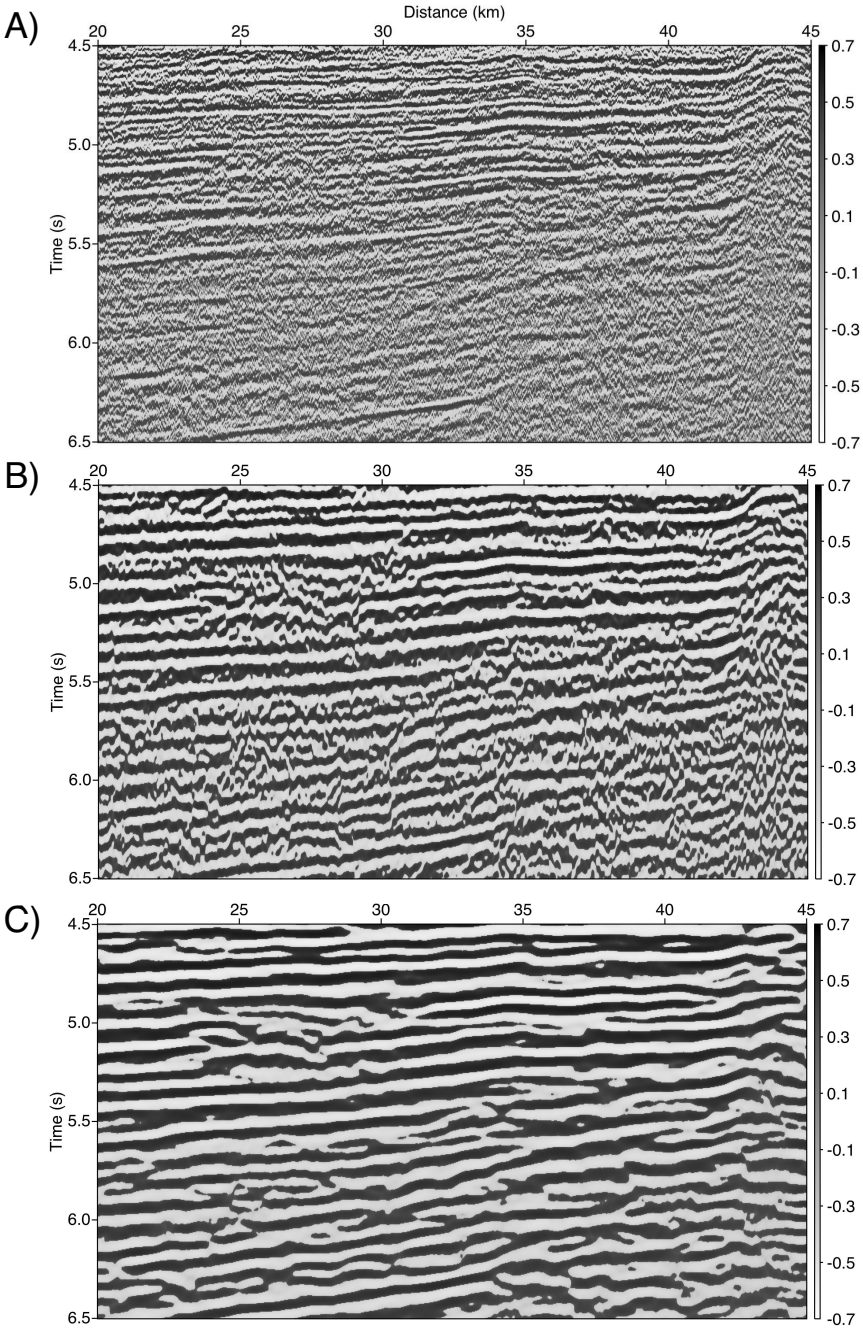

Figure 2.8: (A) A portion of MCS Line 6 that is located near the beginning of the seismic profile (Figure 2.2, box A). CWT coefficients for these data are shown for frequency 10.5 Hz and (B) wavelength 149 m and (C) wavelength 3 km.

31.5 Hz, where the frequency spectrum has its maximum, in Figure 2.9. In this case, we evaluated the CWT coefficients for wavelengths 50 m and 994 m, values that keep the same aspect ratio of the 2-D wavelet as the parameters utilized at 10.5 Hz. Because frequency is increased by a factor of three approximately, the wavelength values are reduced by the same factor to keep the same ratio between period and wavelength. The smaller wavelength produce an image that is very similar to the original seismic image (Figure 2.9B). On the other hand, the coefficients at a wavelength of 994 m are not affected strongly by the random noise in the image and the reflectors are more continuous and easier to interpret even at two-way times from 5.5 to about 6.5 s. Similar effects were seen in the tests on the synthetic test image (Figure 2.6), supporting the conclusion that the features seen in the figure are present in the original image, though obscured by noise. It is possible that some of the apparent reflectors could be associated with multiples or similar effects.

Comparisons of these results with conventional bandpass filtering to enhance reflection signals and suppress incoherent noise illustrate the differences in the operation of the wavelet approach (Figure 2.10). For example, a bandpass filter centered on 10 Hz produces a section that is similar to the CWT coefficients generated for 10.5 Hz and wavelength 149 m (compare Figures 2.8B and 2.10B). The filtering applied a zero-phase filter with a sine-squared taper, utilizing corner frequencies 3, 8, 12, and 20 Hz. The similarity of images is expected, since the bandpass filter operates on individual traces, and the wavelength of 149 m for the CWT includes a comparatively small number of traces. Both also will emphasize signal content on traces near the same frequency. However, the CWT approach has the potential of emphasizing features of different spatial scales as well. Though the wavelength of 3 km is too long compared to the relatively small features of interest in these images (Figures 2.8C), other values may provide important comparisons with small

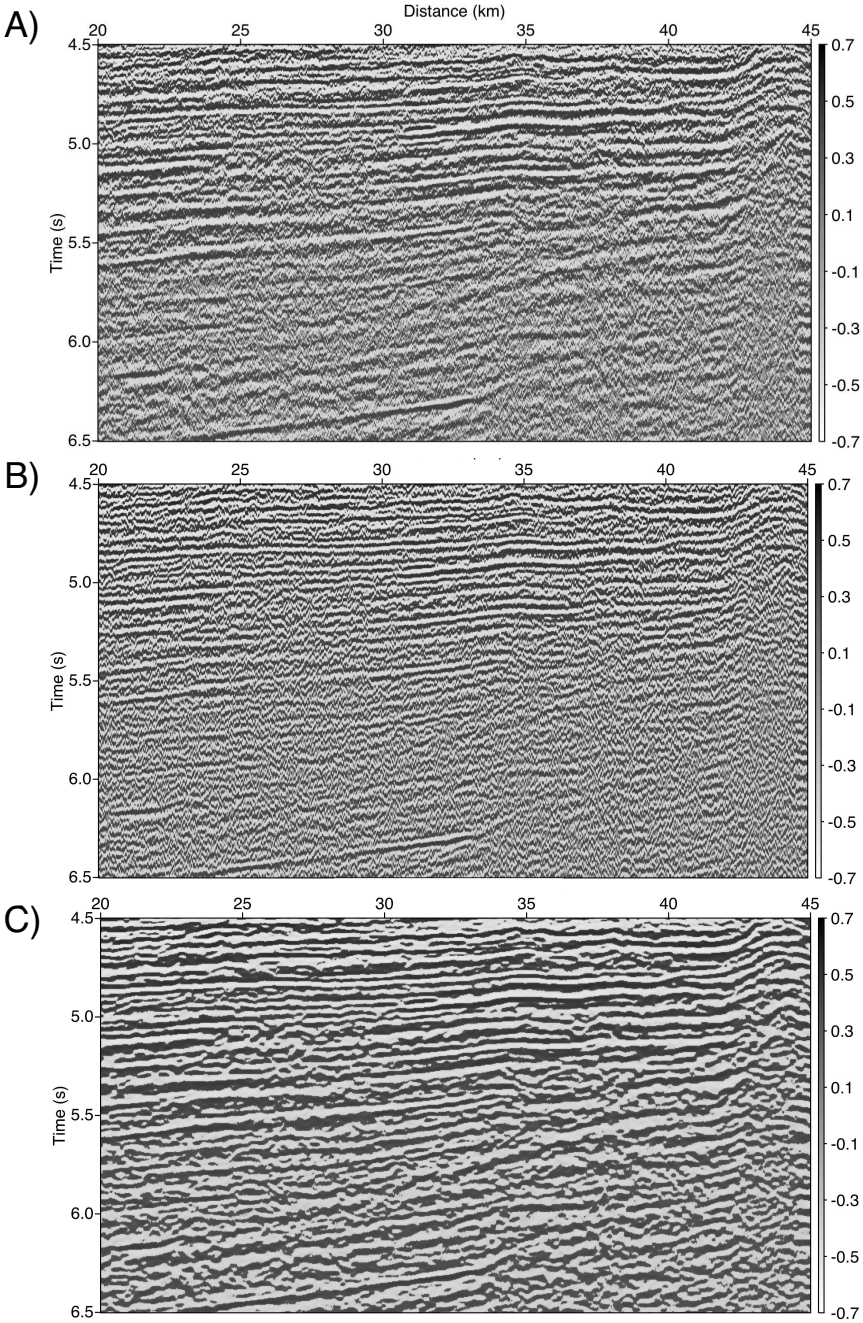

Figure 2.9: (A) A portion of MCS Line 6 that is located near the beginning of the seismic profile (Figure 2.2, box A). CWT coefficients for these data are shown for frequency 31 Hz and (B) wavelength 50 m and (C) wavelength 0.99 km. The wavelengths are smaller than for the low frequency results in Figure 2.8 to keep the wavelet aspect ratio σ unchanged.

wavelength images or bandpass filters. On the other hand, applying a bandpass filter with a higher frequency range is less satisfactory (Figure 2.10C). The filter in this case applied corner frequency values of 12, 20, 40 and 55 Hz. While some noise is suppressed, it is difficult to extract signal content near 30 Hz and avoid an increasingly ringy image in some areas. The CWT coefficients, on the other hand, are able to measure signal near 30 Hz without dinginess, and in this case, the longer wavelength image produces more coherent reflectors while suppressing noise at high dip angles (Figure 2.9). While the bandpass filter approach may be satisfactory in some cases, the CWT measures allow for easier detection of signal over specific, narrow frequency ranges while also allowing for straightforward study of frequencies at various wavelengths.

The second portion of Line 6 that we examine, from 45 km to 70 km, is more geologically complicated (Box B, Figure 2.2). It passes near the center of the Tamu Massif where it is expected that basement reflections may be less continuous because it is near the center of eruptions where flows may be less continuous (Figure 2.11). We can observe that there are two hazy zones from 47 km to 52 km and 64 km to 66 km expressed as approximately vertical features where amplitudes of horizontally coherent reflections are reduced. Figure 2.11 displays the 2-D CWT result at a frequency of 10.5 Hz and horizontal wavelength of 149 m. Compared to the original seismic section, the transformed image shows higher lateral reflector continuity in many regions. Arrows mark several locations where such features can be identified. Nonetheless, regular, parallel reflections are not easily identified, especially in comparison with the previous example where a number of parallel reflections suggest repeated, laminar lava flows (Figures 2.9, 2.9). While some indication of this difference in structure is evident without the application of the CWT, the absence of such features in the CWT result, even with improved signal-to-noise ratio, helps to

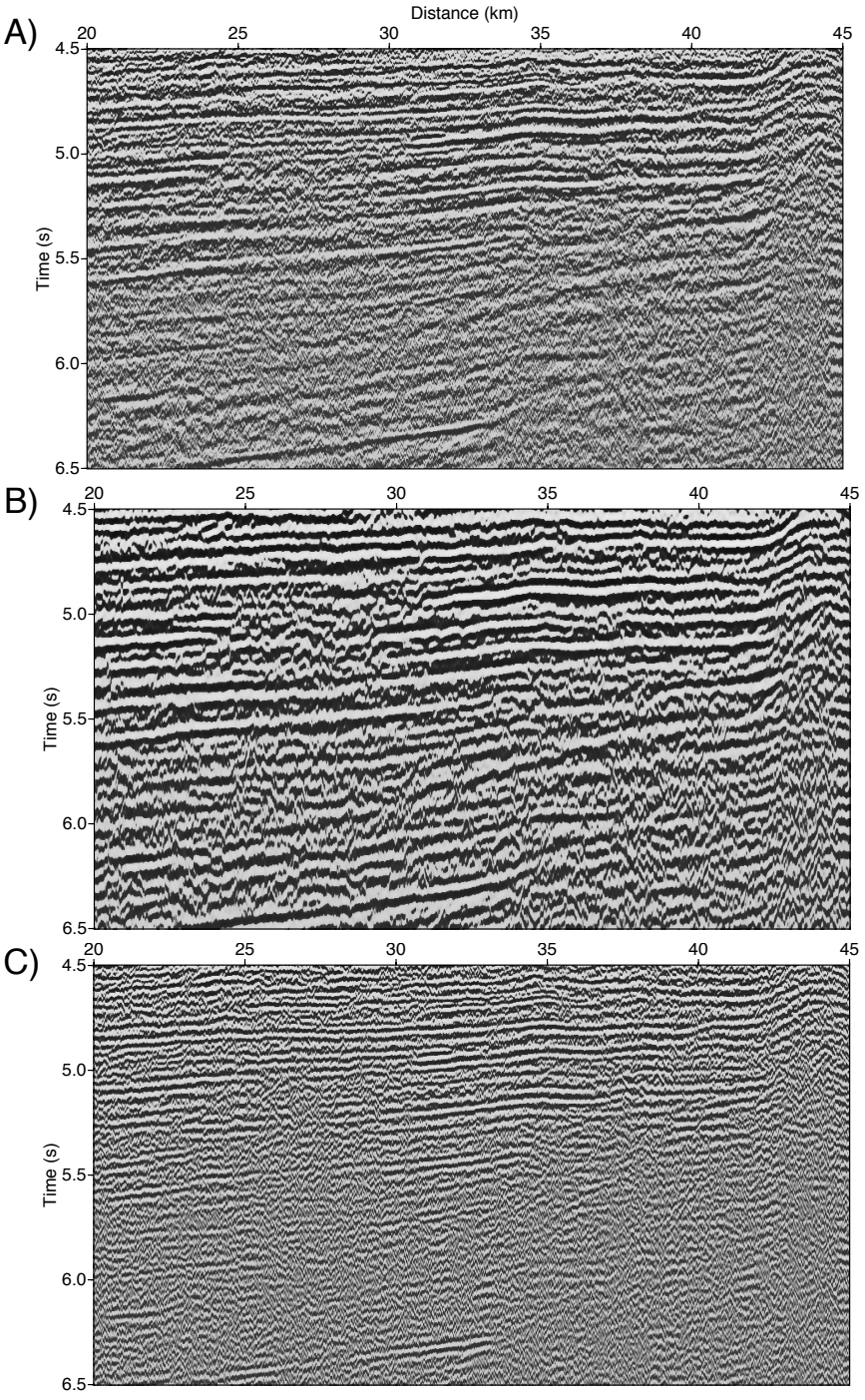

Figure 2.10: Comparisons of (A) portion of MCS Line 6 that is located near the beginning of the seismic profile (Figure 2.2, box A), with bandpass filtered versions of the data (B) from 8 to 12 Hz and (C) from 20 to 40 Hz. Additional details regarding filter specification are provided in the text.

confirm long parallel reflectors are not simply obscured by noise.

2.4.2 CWT applied to line 5

The second seismic line, Line 5 (Figures 2.1, 2.3) extends from a point near the center of the plateau down the west side of Tamu Massif. This image should thus sample lava flows descending the flank. As with Line 6, we concentrate on two portions of the line. The first segment of Line 5 extends from 20 km to 45 km (Figure 2.12), and the image suggests dipping events with two-way travel times up to around 6 s, which is consistent with the lava flows trending downslope from the summit. The section has a relatively low signal-to-noise ratio, however, and includes some very steeply dipping artifacts. Because of this high noise level, we present CWT coefficients computed for larger wavelengths, as the transform for short wavelengths did not improve the image. For simplicity, we continue to apply $\theta = 0$. Specifically, at 10.5 Hz, Figure 2.12B shows coefficients for a wavelength of 3 km, a value that emphasizes the lateral continuity. The results for 31.5 Hz were computed for wavelength 994 m to maintain the same aspect ratio (Figure 2.12C).

At the lower frequency, the dipping reflectors in the upper portion of the image become more obvious (Figure 2.12B). Reflector continuity in the lower part of this 10.5 Hz section is still difficult to follow, but reflecting layers are observed, whereas they are virtually absent from the original section. Similar observations apply to the wavelet coefficients for 31.5 Hz (Figure 2.12B). Vertical resolution improves with higher frequency, as would be expected, but the continuity of reflectors is reduced, especially in the deeper section.

In the second example extracted from Line 5 (Figure 2.13A), the original seismic image is difficult to interpret. There are some reflections visible with lengths around 5 km, such as between 105 and 110 km, with two-way time of about 6.7 s. However,

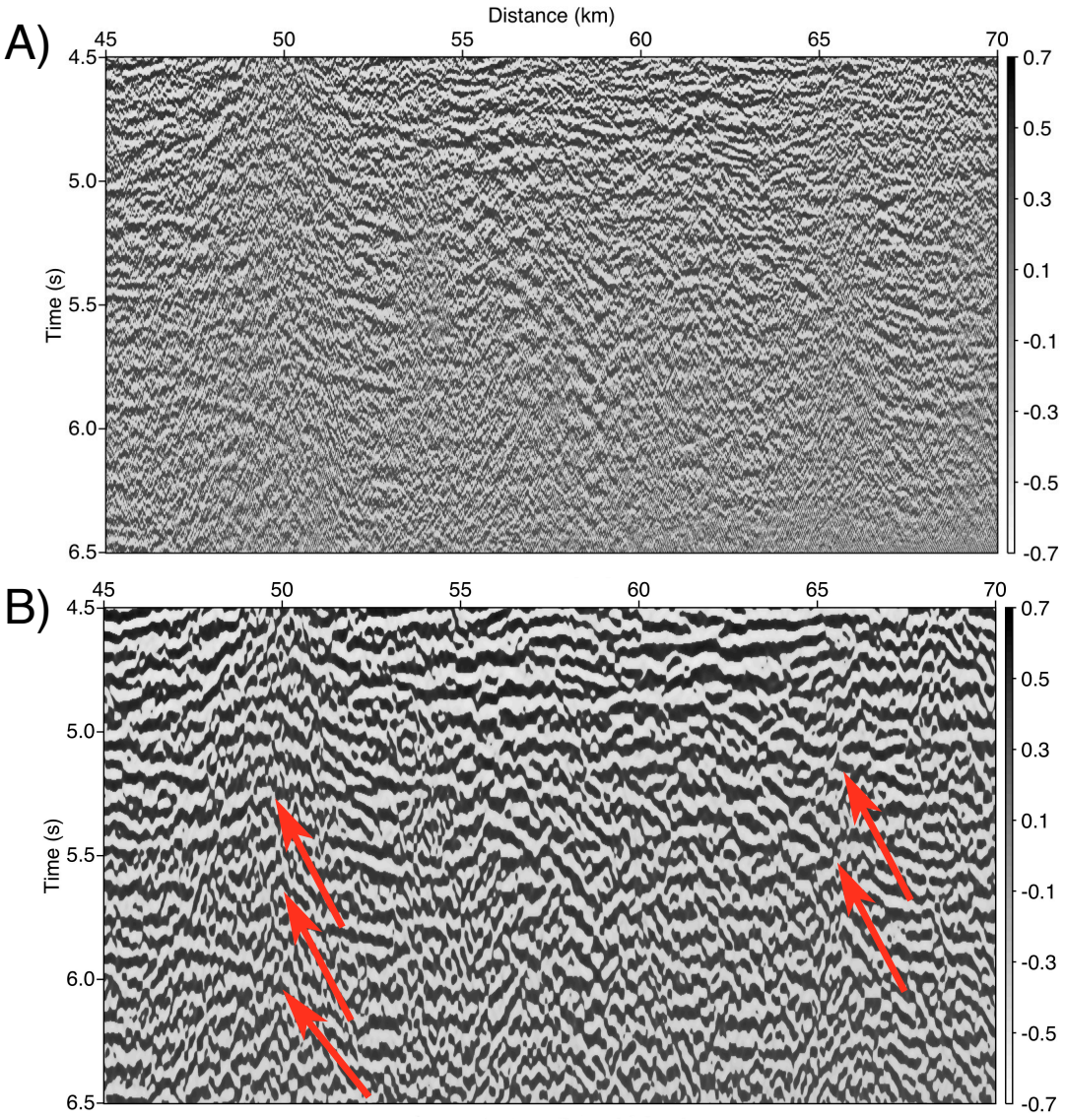

Figure 2.11: (A) A subset of the seismic image from Line 6 passing over the central portion of the plateau (box B, Figure 2.2). (B) 2-D CWT coefficient computed for frequency 10.5 Hz and horizontal wavelength 149 m. Arrows mark regions where reflectors are easier to identify in the coefficient images.

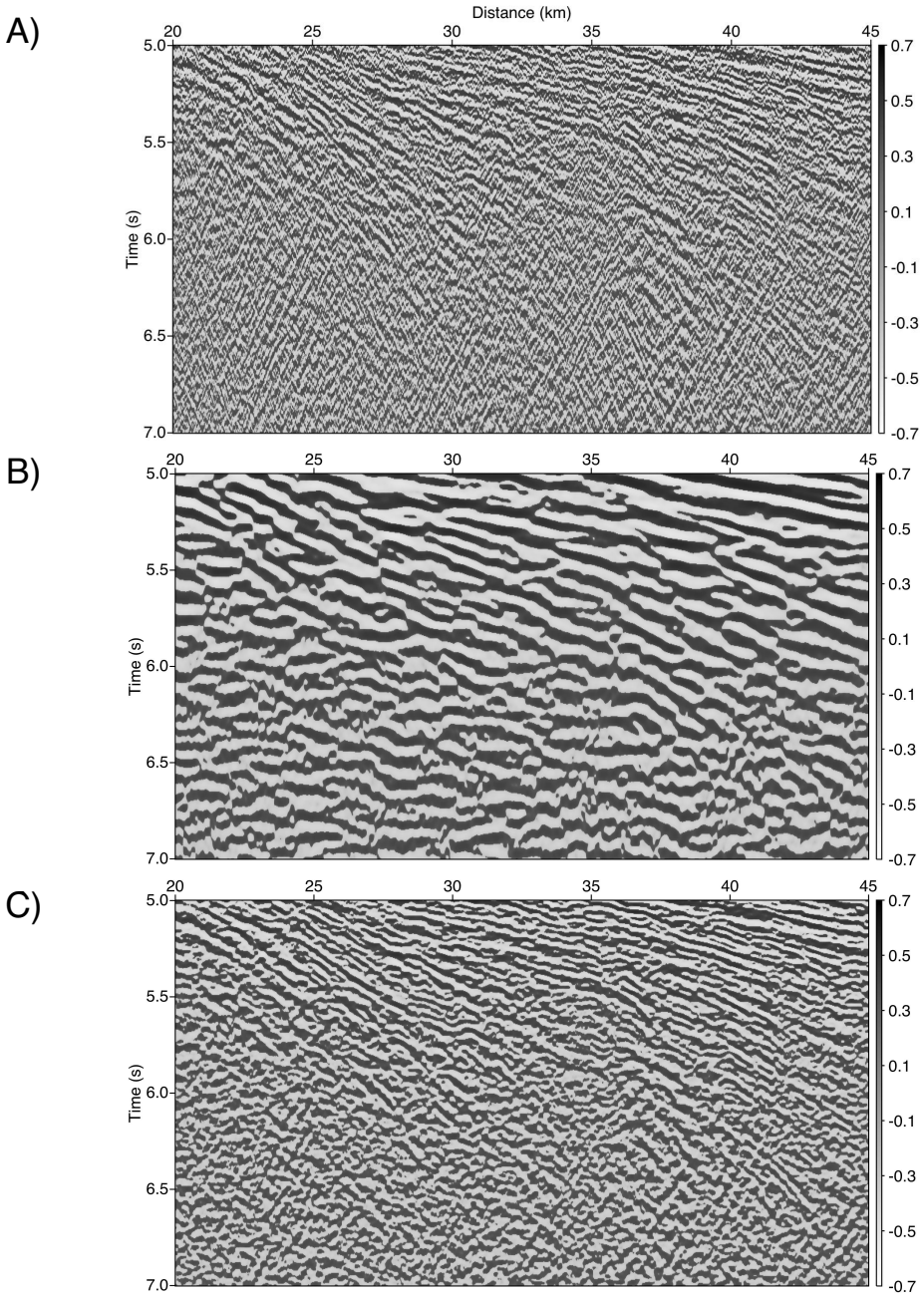

Figure 2.12: (A) A portion of the seismic profile Line 5, from 20 km to 45 km (box C, Figure 2.3). 2-D CWT coefficient computed for (B) frequency 10.5 Hz, horizontal wavelength 3 km, and (C) frequency 31.5 Hz, horizontal wavelength 0.994 km.

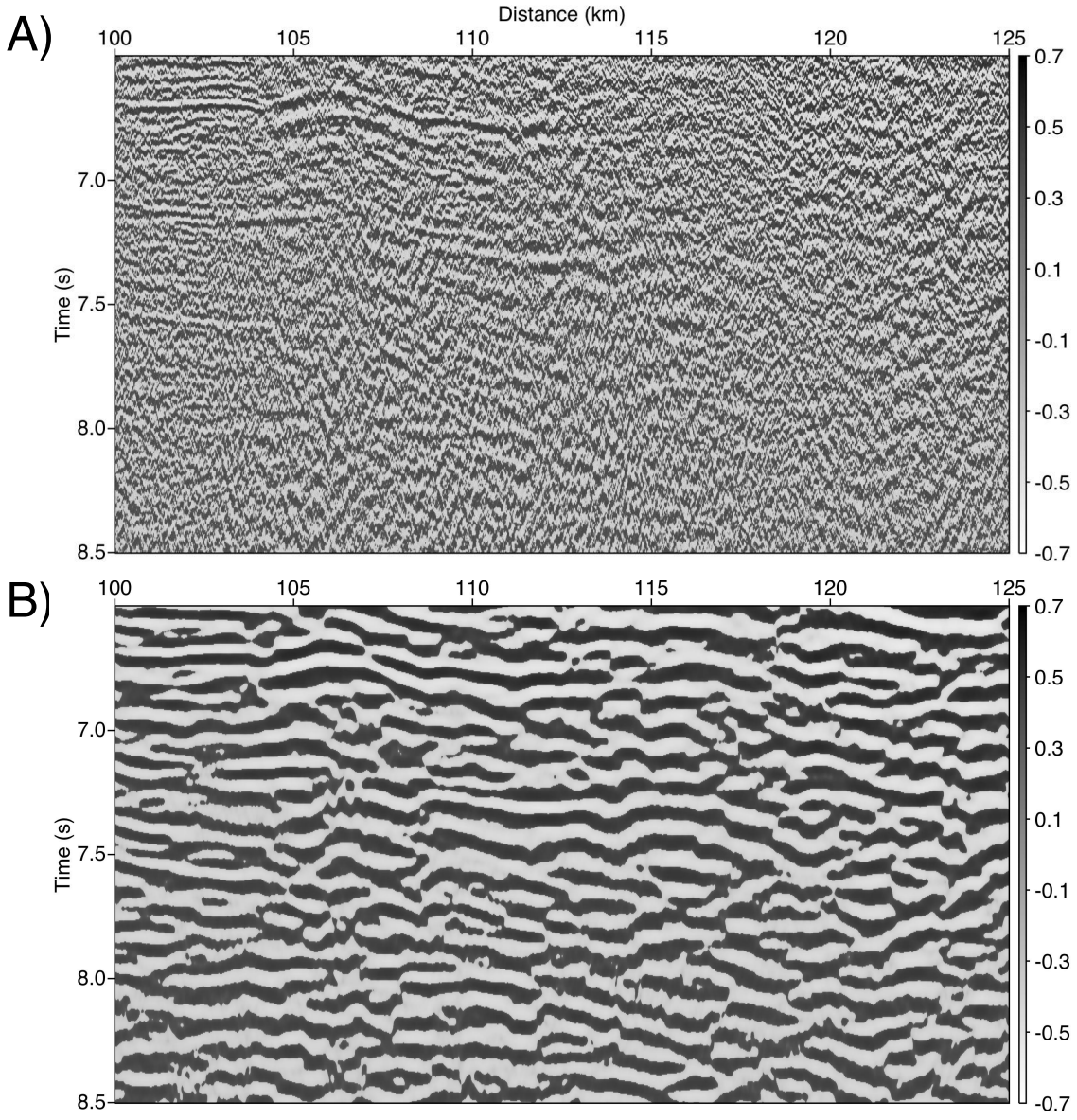

Figure 2.13: (A) A subset of the seismic profile Line 5, from 100 km to 125 km (box D, Figure 2.3). (B) 2-D CWT coefficient computed for frequency 10.5 Hz, and horizontal wavelength 3 km.

more incoherent energy with low horizontal continuity is present in most of the image. This part of the data corresponds to the lower flank of the Tamu Massif, where we do expect small and discontinuous lateral events, but the low signal-to-noise ratio hinders interpretations. We again show results from the low frequency of 10.5 Hz with a horizontal wavelength of 3 km (Figure 2.13B) because that combination was most effective in reducing the amplitude of the spatially discontinuous and laterally incoherent energy in the previous example. The 2-D CWT images show features that can be interpreted as several faults, which are hard to identify in the original image. For example, there is a discontinuity beginning at the upper right corner of the image and extending down to the left at an apparent dip of about 45 degrees in the figure. The true dip is much less, given the vertical exaggeration in the figure. Similar patterns suggesting faulting is present beginning at the top of the section at a distance of 105 km and 120 km. Both features extend down to the left. Comparing to (Figure 2.13A), the original seismic image is dominated by much less spatially coherent energy, and because it is difficult to identify laterally continuous reflectors, it will also be harder to locate potential faults.

2.5 Discussion

The CWT results show the potential value of this approach in facilitating interpretations of data from geologically complex regions such as Shatsky Rise. In general, the coefficient computed by the transform at a specific pair of values for distance along the seismic profile and two-way traveltime is a measure of the energy present in the seismic image for a chosen frequency and wavenumber. As long as noise or artifacts have different frequency and wavenumber, a display of this coefficient in the same format as seismic data can therefore emphasize the image content associated with reflections from geologic features such as massive lava flows more

effectively than the original, noisy image. For example, Figure 2.8 displays the coefficient calculated for the relatively low frequency of 10.5 Hz, and the coefficient values are strong for a number of intra-basement reflectors appearing from 5.5 s to 6.5 s that are almost completely hidden in the original data image (Figure 2.8A). These reflectors have lengths approaching 20 km. Application of the CWT with a longer wavelength produces an image with greater lateral continuity of reflection amplitudes (Figure 2.8C) though this likely minimizes natural variation in reflection amplitude. Arguably many of the trends associated with the longer reflectors may have been detected even in the original image. However, one example of a relatively significant change can be seen at the distance of 35 km and two-way times of about 5.8 s. In the original image, there is some indication of reflecting features, but the CWT image for the wavelength 149 m produces much more similar reflection amplitudes that help to see the geometry of the reflector without interference from the less coherent signal in the image. Similarly, between distances of 25 to 30 km, around 6.5 s two-way time, both the original image and the CWT result show a fairly obvious reflector. In the CWT image, we can also see a more irregular reflector that appears to pinch out around 35 km, an observation we did not identify in the original image. Also, a careful examination of the CWT image, especially for the wavelength 149 m (Figure 2.8B), reveals an interesting arclike reflection pattern at distances around 25 to 28 km, with two-way travel time of about 5.1 s. We suggest that it is much more difficult to identify this dome-like bulge in the original image and that it provides evidence for a possible local accumulation of lava during an eruption. This especially is a new result that was not obtained during original interpretations of these seismic images (e.g., Zhang et al., in this volume).

Generally similar trends result for the 2-D CWT computed for different wavelengths at 31.5 Hz (Figure 2.9). Results for the very short horizontal wavelength of

50 m are actually fairly similar to the original seismic image, since the noise content has similar scales (Figure 2.9B). In contrast, when the transform coefficients are computed for the longer horizontal wavelength of 994 m, the short wavelength noise does not affect the results, and the basement reflectors have increased lateral continuity (Figure 2.9C). These intra-basement reflectors are interpreted as long lava flows emanating from the center of the plateau. Therefore, one can vary the horizontal wavelength of the wavelet to maximize the interpretation and to better identify expected geologic features to the seismic image. In general, we find that the combination of CWT coefficient images for 10.5 Hz and 149 m wavelength and 31.5 Hz and 990 m wavelength provides the greatest contributions to additional insights into subsurface features in our interpretations. In general, we would expect that examining CWT results for various combinations of frequency and wavenumber will be important for understanding and explaining the images and for drawing conclusions on geological issues.

Comparisons to the synthetic test image help to confirm these interpretations and to demonstrate how to interpret them reliably. We recall that for lower frequencies, the transform for a long wavelength can help to clearly locate reflecting features and to suppress the effects of noise (Figure 2.5). However, the ability to resolve individual reflectors is reduced. We can expect the same pattern for the field data, and this is essentially what we see in Figure 2.8C. On the other hand, the longer wavelength results at the higher frequency have suppressed the effects of noise but still allow some inference of lateral variations in reflector amplitude.

The second area of Line 6, which is near the summit of the plateau is more geologically complicated and has fewer long, continuous reflectors associated with flows (Figure 2.11). It is also important to note that it is found underneath a cone-like feature at shallower depths, and diffractions or other waves generated by this

cone affect the image (see Figure 2.2). As a result, the image shows many short intra-basement reflectors as well as significant noise. Unlike the results for the first portion of Line 6, the 2-D CWT results calculated with the low frequency of 10.5 Hz include a larger number of relatively short reflection events instead of long, continuous reflectors (Figure 2.11B).

The first area of Line 5 to which we applied the CWT also displays some shallow dipping reflectors ($0.5^0 - 1.0^0$), which in this case are similar to sedimentary clinoform layers (Figure 2.12) (Zhang et al., in this volume). The 2-D CWT coefficients for the low frequency of 10.5 Hz and horizontal wavelength 3 km show clear reflectors and intra-basement reflectors with two-way traveltimes from 6.0 s to 7.0 s, while values for the high frequency 31.5 Hz and wavelength 994 m are not much easier to interpret than the original image. The lower frequency CWT result is more effective for the complicated geological structure in this case. The noise and artifacts that hinder analysis of the images are not well correlated over large distances or with time, so they will have minimal impact on the coefficients for lower frequency and longer wavelength.

The second area is difficult to interpret (Figure 2.13A) since there is a lot of noise as well as shorter and more discontinuous reflection events. To improve the interpretation, we calculate the 2-D CWT at low frequency of 10.5 Hz and long horizontal wavelength of 3 km. Figure 2.13B shows intra-basement reflectors clearly as well as some faults. For example, faults can be observed at position of 118 km with two way travel times from 6.5 s to 7.5 s and at 123.5 km with two way travel-time from 6.75 s to 8.1 s. These faults may be the results of ridge-related rifting or by differential subsidence (Zhang et al., in this volume). The proposed faults are hard to find in the original image, and identifying them is another important benefit of utilizing the CWT images.

These results therefore provide several examples of new geological insights that result by applying the CWT to the seismic images, though systematic analysis to make conclusions regarding Shatsky Rise will clearly require applications of the CWT to entire seismic lines. Nonetheless, there are suggestions of some important new results already. Based on initial interpretations of the multichannel seismic and samples from core sites, Sager et al. (2013) suggested that Tamu Massif is a single, massive volcano and that therefore it is composed of lava flows extending uniformly away from a central site (see also Zhang et al., this volume). The layers would therefore be subparallel in all directions. Complexities such as the bulging dome identified in Line 6 suggest additional complexity that would motivate revision of the hypothesis. An important goal for future research is therefore to carry out more detailed processing and interpretation to better measure the geometry and distribution of reflecting features such as lava flows around Tamu Massif.

2.6 Conclusions

In this research topic, we propose the application of 2-D CWT to characterize the basement of oceanic plateaus such as Tamu Massif of Shatsky Rise. We use the 2-D normalized anisotropic Mexican hat wavelet to make quantitative comparisons of results with different frequency and wavenumber. We note that it is important that we apply the normalization constant mentioned in the discussion of equation 2.8 to allow quantitative comparisons of coefficients for different wavelengths and frequencies. The results of the 2-D CWT analysis on recent marine seismic data acquired over Tamu Massif of Shatsky Rise help better reveal the structure and lateral variation of the basement. All of the images from 2-D CWT show that the amplitude of incoherent noise is reduced in comparison to that of laterally continuous events. While in some cases conventional bandpass filtering may be adequate for facilitating

interpretation of images, the CWT will be a good option when the enhancement of lateral continuity and minimization of signal with low coherence is required. The test applications also show that is important to review CWT results with different combinations of frequency and wavelength to select optimal values. In several cases, the CWT provides benefits for interpretation by varying the horizontal wavelength parameter to better correlate lateral reflectors which are associated as intra-basement reflectors. On one line, the 2-D CWT allowed detection of possible faults not observed in the original image, and in another example new dome-like features suggesting lava intrusions were detected in the CWT image. These examples help support the role of this approach in interpreting seismic images acquired in areas such as the Shatsky Rise.

3. MULTI-SCALE ANALYSIS THE SURFACE ROUGHNESS OF THE MINERALS

3.1 Introduction

Geochemical reactions on mineral surfaces are important for a variety of studies, including the movement of pollutants and ground water in acquirers. In addition, the flow of hydrocarbons in reservoir formations is influenced by geochemical reactions such as adsorption or absorption on pore surfaces. The relevant chemical processes are strongly related to surface energy and the ability of exposed molecules to react with materials in fluids. In particular, surface roughness is very important, because a rough surface will typically have a much larger number of molecules exposed with unfilled bonds (White and Brantley, 2003; Becker et al., 2001). Such molecules with missing neighbors and unfilled bonds all have a greater free energy and can react more readily. Therefore, it is very important to study the characterization of surface roughness and its evolution during chemical reactions to better understand implications for the environmental or hydrocarbon applications. An enhanced knowledge of the surface texture could lead to better understand the geochemical reactions and environmental effects on the mineral surface.

The problem of studying surface texture and developing quantitative measures for surface roughness at various spatial scales has been a challenging task (Reed and Dubuf, 1993; Tuceryan and Jain, 1998). There is much previous work on the characterization of texture (Thomas, 1982; Stout, 1993; Whitehouse, 1994), and typical texture analysis is calculated at single spatial scale. In addition, the previous methods are only applicable for stationary spatial patterns that show no variation in scale with position. However, mineral surface textures are non-stationary and

vary laterally. Therefore, the 2-D CWT is a good candidate for the study of the spatial frequency content of such data. The 2-D CWT has been successfully applied to characterize painted surfaces(Mezghania, 2011), where the surface roughness is understood as any surface features with wavelength less than 0.8 mm. This surface roughness measure is meaningful only for painted steel sheet surface (Mezghania, 2011). Another similar work is to observe the surface finishing of steel based on decomposition of surface topographic by 2-D CWT (Zahouani et al., 2008), where the surface roughness is defined as following

$$R_a = \frac{1}{N} \sum_{i=1}^{N} z_i \tag{3.1}$$

Where z_i is the element elevation, and the sum is taken over the entire of steel surface sample. In this work, the author calculated the surface roughness of their steel sample and the surface roughness parameter is 0.9 μm. This formula is also used to calculate the surface roughness of material measured in atomic force microscope (Namba et al., 2000). The 2-D CWT has not yet been applied to study mineral surfaces to the best of our knowledge.

In this dissertation, we carry out the decomposition of the surface topography of mineral surfaces by using 2-D CWT with a normalized Mexican hat wavelet, with the aim of gaining information providing insights into the geochemical and weathering effects on the mineral surface. There is no unique formula to calculate the surface roughness. Since our surface elevation data for the minerals are measured by confocal microscopy, we compare results from CWT to roughness measures computed using a formula which is introduced by Lange et al. (1993). The details of the formalism are given in section 3.3. We first calculate the surface roughness of each mineral sample, then calculate the 2-D CWT coefficients at different wavelength. We study the

characterization of 2-D CWT coefficients which are associated with the topographic components at particular wavelength.

Below we first describe the confocal microscope system that is used to acquire the surface height data for mineral samples of interest. Some errors can occur in measurements, and these errors create "spikes" (artifacts) on the mineral surface. We will show how we remove the spikes by using a 2-D median filtering method. We review the formula of the surface roughness which is used in building topographic of confocal microscopic, and we then calculate the surface roughness for each mineral sample. Finally, we present data and 2-D CWT analysis for two samples of the mineral Fe_2O_3 and three samples of calcite. The results of decomposition of the mineral surface by using 2-D CWT are discussed.

3.2 The confocal microscope

In this research subject, we use confocal microscopy to obtain three-dimensional descriptions of the minerals samples. We will describe how the confocal microscopic work and the way topographic map of mineral sample is obtained.

Confocal microscope is optical device which have ability of obtaining the bright images in focus region while causing all out of focus regions to be dark (Lange et al., 1993). The Figure 3.1 shows the typical image at certain surface height value of the sample mineral of Fe_2O_3. The topography image of the samples are created by assembling a series of optical sections (Figure 3.2). Each optical section is presented at different focal plane. Therefore there is no limitation of the depth field in the measurement by using confocal microscopes (Lange et al., 1993). This is the reason why confocal microscope is a useful method to image non-flat materials (Lange et al., 1993). The intensity of each pixel in the image depends on each optical section as the image can be in or out focus (Figure 3.3). The topographic map of the mineral

Figure 3.1: Typical image obtained in confocal microscopic, mineral sample Fe_2O_3 . The grey scale image identifies the portion of the surface at a specific elevation value.

obtained by using confocal microscopy is a digital image where each pixel represents the vertical value (Lange et al., 1993).

The actual surface of the mineral sample was calculated by using the "Fiji" software package to generate the geometric construction of the surface from the microscope data. Figure 3.4 shows that the surface of mineral Fe_2O_3 sample displays a number of single sample errors or glitches that we will refer to as spikes. The values of these spikes are very different from the neighboring values. For example, the value of the spikes is about 1 μ while the neighboring values are near 30 μ. These spikes are likely due to some artifact of the confocal microscope measurements, and the surface with these spikes does not reflect the true roughness of the surface of the mineral. Therefore one needs to remove these spikes before carrying out surface analysis. We remove these spikes by following the 2-D median filtering method. The reason is that median filtering is a nonlinear operation and more effective than convolution

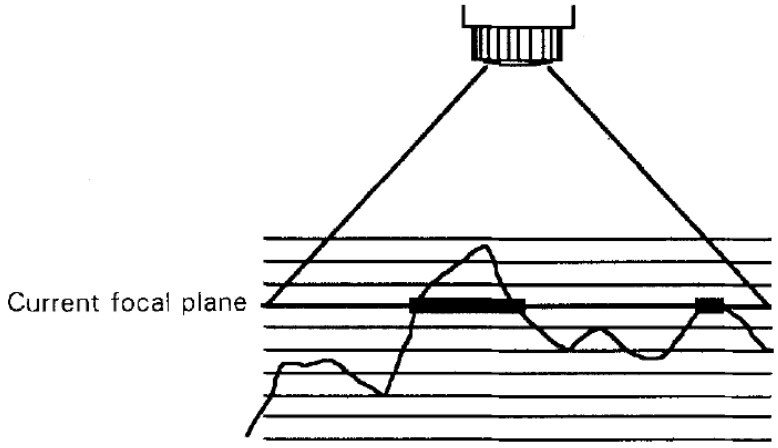

Figure 3.2: Optical sections with confocal microscope (Lange et al., 1993).

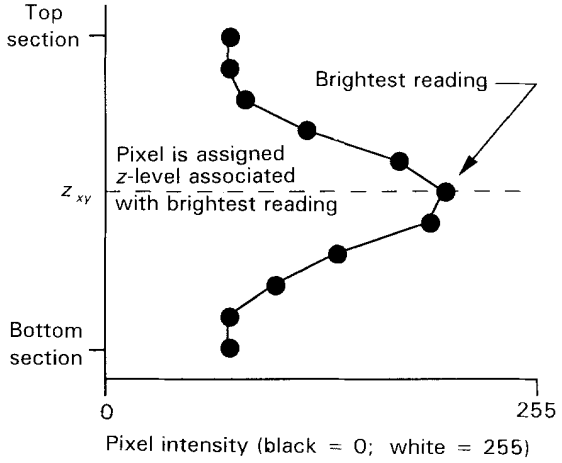

Figure 3.3: Typical pixel intensity as function of optical section (Lange et al., 1993).

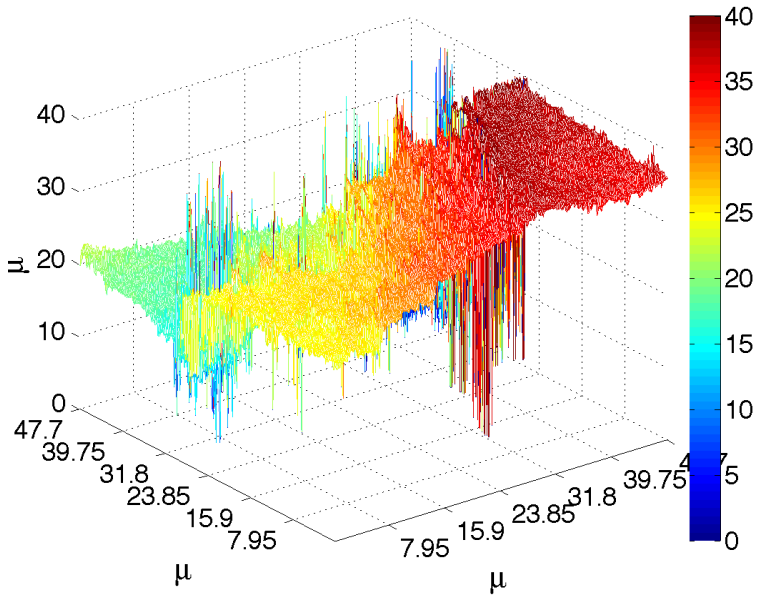

Figure 3.4: Topographic map of Fe_2O_3 mineral sample with spikes

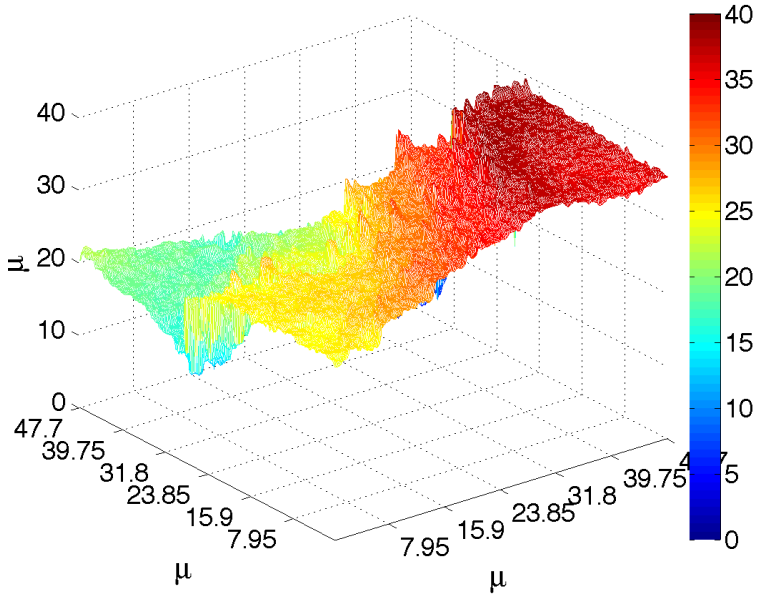

Figure 3.5: Topographic map of Fe_2O_3 mineral sample without spikes

(Matlab 2012b). The algorithm of 2-D median filtering is that with a given window matrix m-by-n running over the 2-D surface data, the height value of the surface pixel is replaced by the median value of m-by-n neighborhood around the corresponding pixel. In our calculation, we select the window matrix is 4 by 4. Figure 3.5 shows the surface of the mineral Fe_2O_3 sample after removing spikes. This operation is applied to each topographic map of mineral sample. In the next sections, all the topographic maps are presented without spikes.

3.3 The surface roughness formalism

Surface roughness, the variation in height of a surface relative to an ideal uniform trend, has had several measurements defined in different fields of research, but there is no unique value. In this section, we summarize the measurement of surface roughness given in detail in Lange et al. (1993). We follow this formalism to calculate the surface roughness of the minerals by using topographic measured in confocal microscopic. The surface roughness is defines as

$$R_s = \frac{\sum A_s}{\sum A_n}, \tag{3.2}$$

whereA_s is the approximate element area of topographic map, and A_n is the nominal element surface area. The sum is over the entire surface. Figure 3.6 illustrates the geometry of element topographic map which is used to calculate the actual surface. The lines segments are calculated by the following equations (Lange et al., 1993)

$$s_{ij} = [s^2 + (z_i - z_j)]^{1/2}, \tag{3.3}$$

but for the line segment s_{13}, the formula is

$$s_{13} = [2s^2 + (z_1 - z_3)]^{1/2}. \tag{3.4}$$

Perimeters are given by

$$p_1 = \frac{1}{2}(s_{12} + s_{23} + s_{13}), \tag{3.5}$$

$$p_2 = \frac{1}{2}(s_{34} + s_{42} + s_{13}), \tag{3.6}$$

and the triangle areas are

$$A_1 = [p_1(p_1 - s_{12})(p_1 - s_{23})(p_1 - s_{13})]^{1/2}, \tag{3.7}$$

$$A_2 = [p_2(p_2 - s_{12})(p_2 - s_{23})(p_2 - s_{13})]^{1/2}, \tag{3.8}$$

and the element surface area is

$$A_s = A_1 + A_2. \tag{3.9}$$

The normal surface area is given

$$A_n = s^2 \tag{3.10}$$

The values of surface roughness of each sample are calculated and presented in each mineral sample figures in section 3.4 to compare to new CWT results. In the next section, we describe the topographic maps of the mineral samples used for study the surface roughness.

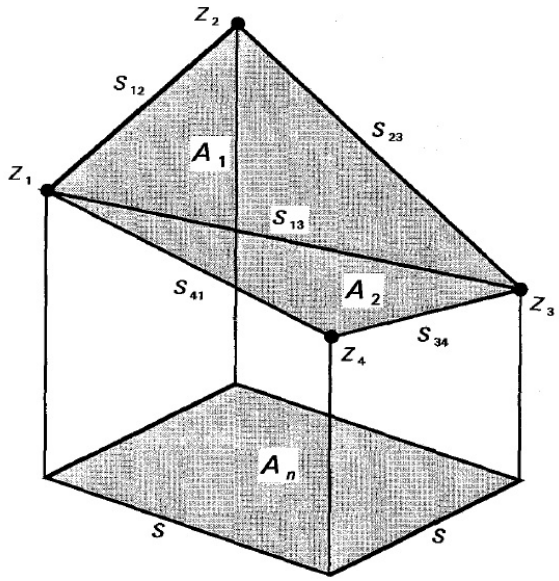

Figure 3.6: Representative area element bounded by four neightbouring pixels in the topographic map (Lange et al., 1993).

3.4 Topographic maps of minerals

In this section, we present the surface mineral datasets measured by confocal microscope. The mineral samples that we study in this dissertation include two samples of Fe_2O_3 and three samples of calcite. In the measurement by confocal microscope, we have 173 optical sections for first Fe_2O_3 mineral sample (sample A, Figure 3.7), 201 optical section for second sample (sample B, Figure 3.8), and 107, 125 and 322 optical sections for calcite in the Figures 3.9, 3.10, 3.11. Note that the number of optical sections for sample C of Calcite (Figure 3.11) is quite large compared to other sample of calcite because the surface of sample C is very rough. It is also important to note that measurements for both Fe_2O_3 samples represent a 300 by 300 grid, but sample A has a horizontal sample interval 2.485 microns, and sample B has 0.159 microns. For the calcite measurements, samples A and B both have 590 by 590 points, while sample C has a 600 by 600 grid. The horizontal sample

intervals for calcites A, B and C are 0.3, 0.295 and 0.147 microns, respectively.

In this dissertation, we study the effect of geochemical and weathering reactions on the surface of the mineral, therefore we collected two different types of mineral surfaces. The first group includes mineral with surfaces that were exposed to weathering, and we can observe the erosion of geochemical and weathering reactions on two samples of Fe_2O_3 mineral (Figures 3.7, 3.8) and two samples of calcite (Figures 3.10 and 3.11). The erosion effects create large fluctuations of the elevation on the surface (Figures 3.7, 3.8, 3.10 and 3.11). We need to determine the location where the most geochemical reactions will occur. These location are associated with the surface energy which is defined as the disruption of inter-atomic bonds (White and Brantley, 2003; Becker et al., 2001).

The second type of mineral surface is from the unweathered material, a fresh crystal surface. Since this is the surface of a fresh cleavage plane from a calcite crystal, we expect to see uniform surface of calcite (Figure 3.9). The topographic map of this mineral is quite smooth compared to other calcite minerals.

3.5 Roughness analysis of surface of mineral samples

In this section, we apply the 2-D CWT method which is presented in Chapter 2 to study the characterization of surface roughness of the each mineral samples as well as the effects of geochemical reactions. We use the 2-D normalized isotropic Mexican hat wavelet (equation 2.5) for all calculations.

3.5.1 Fe_2O_3 mineral samples

The surface elevation maps for two samples of Fe_2O_3 mineral are given in Figure 3.7 and 3.8. The size of sample A (745.5 μ) is larger than the size of sample B (47.7 μ). The topographic maps of these Fe_2O_3 samples show the effects of geochemical reactions on the mineral surfaces. The surface roughness is 1.2132 for sample A and

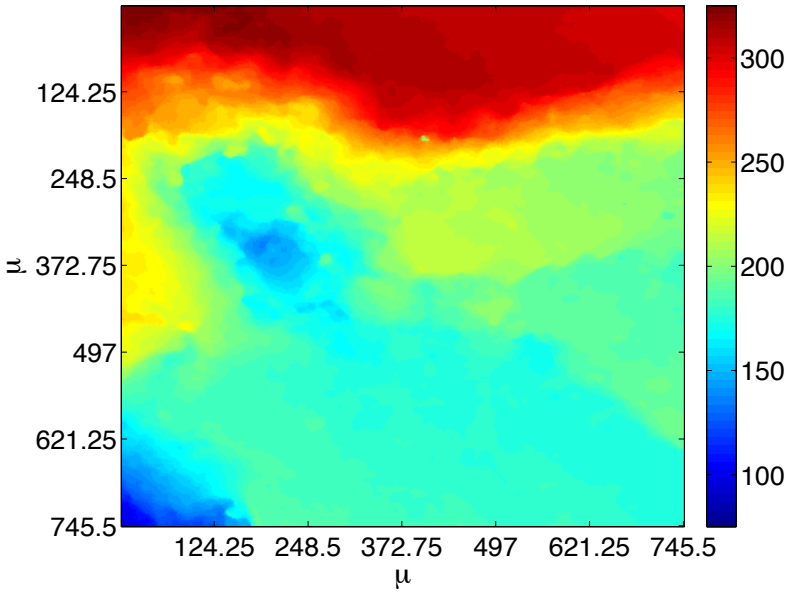

Figure 3.7: Sample A: Fe_2O_3 sample, with computed surface roughness parameter $R_s = 1.2132$

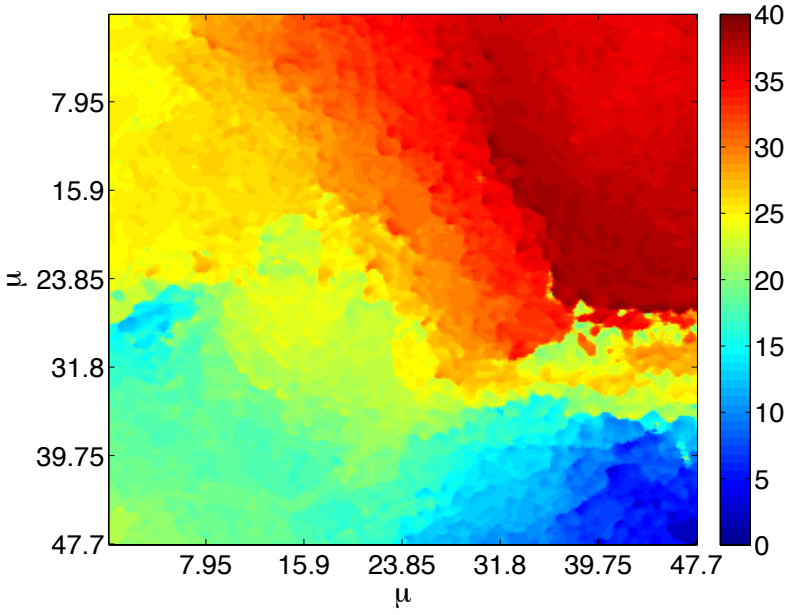

Figure 3.8: Sample B: Fe_2O_3 sample, with computed surface roughness parameter $R_s = 2.8007$

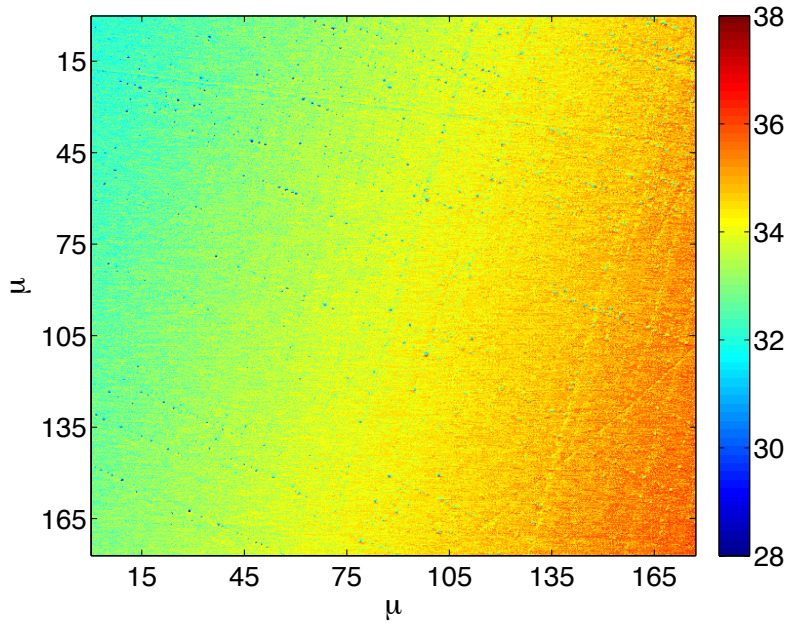

Figure 3.9: Sample A: calcite sample, with computed surface roughness parameter $R_s = 1.1774$

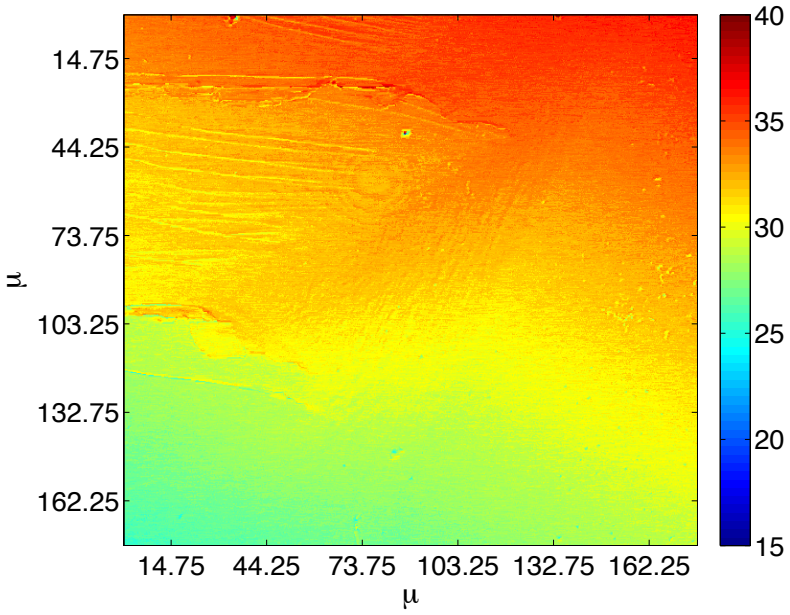

Figure 3.10: Sample B: calcite sample, with computed surface roughness parameter $R_s = 1.2499$

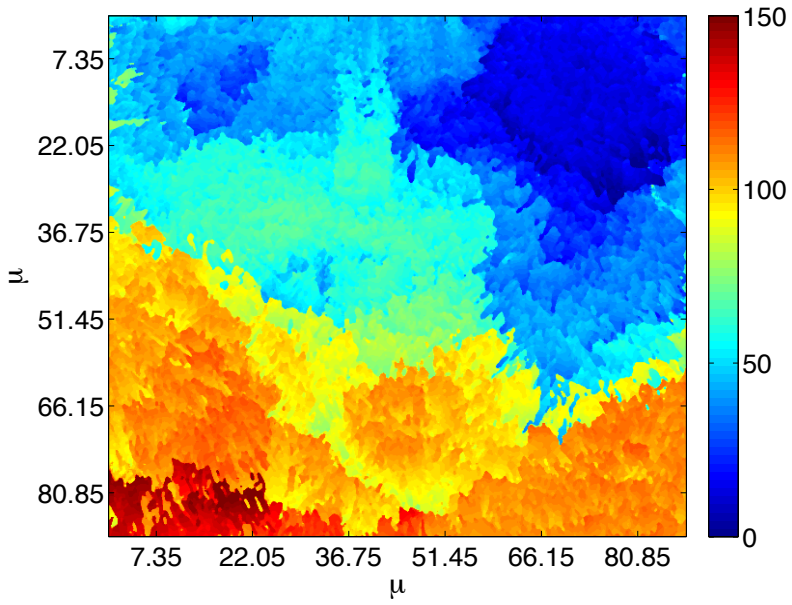

Figure 3.11: Sample C: calcite sample, with computed surface roughness parameter $R_s = 13.2589$

2.8007 for sample B by using equation 3.2. We can observe that the surface of sample B is more rough than the one in sample A.

3.5.1.1 Sample A of Fe_2O_3 mineral

The mineral surface of Fe_2O_3 mineral sample in Figure 3.7 displays very high elevation at the right upper corner, and very low elevation in the right lower corner. The surface is not smooth due to the weathering processes. The surface component associated with 2-D CWT coefficient in Figure 3.16 calculated at wavelength of 368.1 μ, which is about half of the sample size, shows that the mineral surface in Figure 3.7 has several major distinct regions. The high elevation areas are represented in red and low elevation as blue and green. At this large wavelength, we can not observe the details of the surface since the surface roughness ($R_s = 1.2132$) is small while Figure 3.16 shows only the surface component at large size associated with the wavelength

of 368.1 μ. Figures 3.13, 3.14 and 3.15 show the 2-D CWT coefficients calculated at different wavelengths of 24.5 μ, 73.6 μ, and 122.7 μ. We see that when the wavelength of the Mexico wavelet increases, the maximum values of amplitude of the 2-D CWT coefficients also increase from 1800 to 3200 and 8000 respectively.

The 2-D CWT coefficient in Figure 3.13 calculated at wavelength of about 24.5 μ, one can identify locations of small objects with high amplitude (red spot) of the topographic map. These objects are hidden in the surface data (Figure 3.7) which are not easy to be identified. This observation can help us to identify the location of chemical and weathering initial reactions since they have high surface energy. These location have the size less than 24.5 μ. When we increase the wavelength of the wavelet to 73.6 μ (Figure 3.14) and 122.7 μ (Figure 3.15), the location of these details spread out as we expect because the 2-D CWT coefficient with larger wavelength can only measure the larger objects on the surface.

3.5.1.2 Sample B of Fe_2O_3 mineral

The second sample of Fe_2O_3 mineral is displayed in the Figure 3.8. We note that this sample is quite small, it is about 1/15 of the size of the previous Fe_2O_3 sample. The topographic map shows the surface of the mineral very rough, with roughness 2.8007 (using equation 3.2). Figure 3.21 shows the 2-D CWT calculated at wavelength of 23.6 μ, which is about half the size of the sample. We can not observe the small surface object because the surface is rough, it forms by small object and and this 2-D CWT coefficient represents the surface component of formed by object at large wavelength. We carry out 2-D CWT calculations at smaller wavelengths of 0.4 μ, 3.0 μ, 7.0 μ. Figures 3.18 shows that at very small wavelength of 0.4 μ, one can observe the location of very small objects with maximum amplitude of 0.7 μ. Other areas of the surface mineral do not contribute much to the roughness since they have

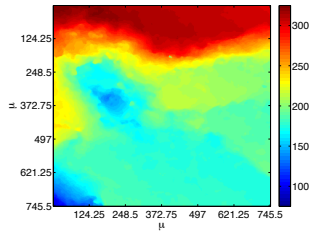

Figure 3.12: Sample A: Fe_2O_3 sample, with computed surface roughness parameter $R_s = 1.2132$

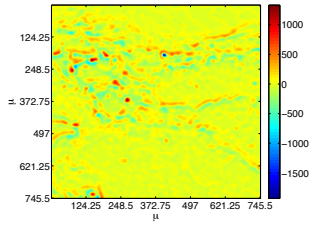

Figure 3.13: Sample A Fe_2O_3 mineral: 2-D CWT calculated at $\lambda = 24.5\ \mu$

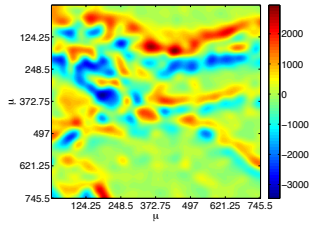

Figure 3.14: Sample A of Fe_2O_3 mineral: 2-D CWT calculated at $\lambda = 73.6\ \mu$

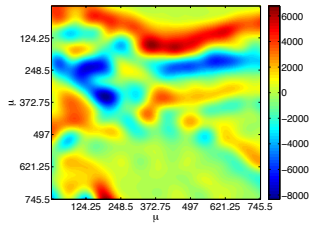

Figure 3.15: Sample A of Fe_2O_3 mineral: 2-D CWT calculated at $\lambda = 122.7\ \mu$

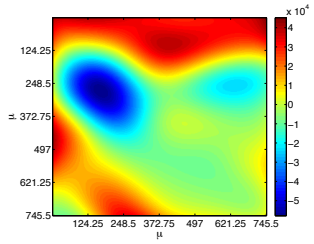

Figure 3.16: Sample A Fe_2O_3 mineral: 2-D CWT calculated at $\lambda = 368.1\ \mu$

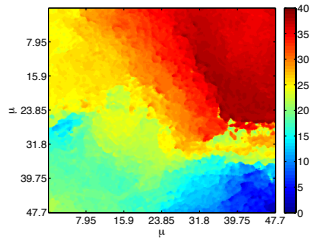

Figure 3.17: Sample B: Fe_2O_3 sample, with computed surface roughness parameter $R_s = 2.8007$

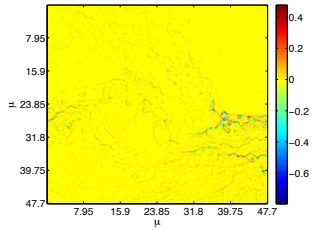

Figure 3.18: Sample B of Fe_2O_3 mineral, 2-D CWT calculated at $\lambda = 0.4\ \mu$

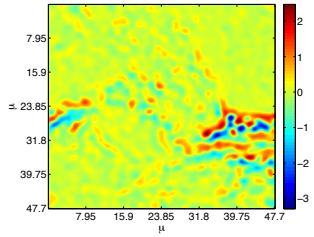

Figure 3.19: Sample B of Fe_2O_3 mineral, 2-D CWT calculated at $\lambda = 3.0\ \mu$

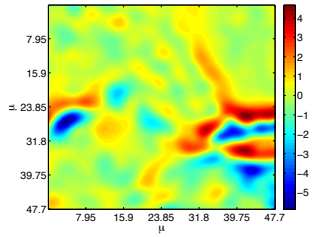

Figure 3.20: Sample B of Fe_2O_3 mineral, 2-D CWT calculated at $\lambda = 7.0\ \mu$

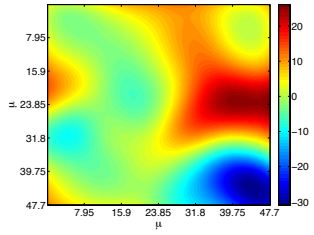

Figure 3.21: Sample B of Fe_2O_3 mineral, 2-D CWT calculated at $\lambda = 23.6\ \mu$

small amplitudes close to zero. These locations displayed red spots are not easy to observe in the original topographic and they have very high surface energy. This observation again help us to determine the initial chemical and weathering reactions on the surface.

When we increase the wavelength of wavelet to 3.0 μ and to 7.0μ the details of the surface will decrease as we expect from the nature of the 2-D CWT analysis. The the maximum amplitude of the 2-D CWT coefficients increase from 3 μ to μ proportionally with the increment of the wavelength from 3.0 μ (Figure 3.19) to 7 μ (Figure 3.20). The details of the surface in Figure 3.18 could explain the weathering process initially occur then spread out (Figures 3.19, 3.20).

3.5.2 Calcite samples

In this section, we present the results of 2-D CWT for the mineral samples of calcite given in Figures 3.9, 3.10, and 3.11 and by using equation 3.2 the surface roughness are 1.1774, 1.2499 and 13.2589, respectively. The sample A represents the fresh cleavage plane surface of the mineral, where there is no geochemical or weathering reaction effect on the surface. Therefore the surface is very smooth and it has smallest value of surface roughness. Sample B and sample C are the samples represents the exposed surface, where we can observe the effects of the chemical and weathering reactions. The surface of sample C is much more rough than the one of sample B, and it is confirmed by the biggest value of surface roughness R_s.

3.5.2.1 Sample A of calcite

This sample is a fresh cut of the calcite therefore there is no geochemical or weathering process on the surface. We expect to observe the topography consistent with a face of a calcite crystal on the surface. The cross section view of the mineral sample is displayed in Figure 3.22. The figure shows stair-step periodic structure.

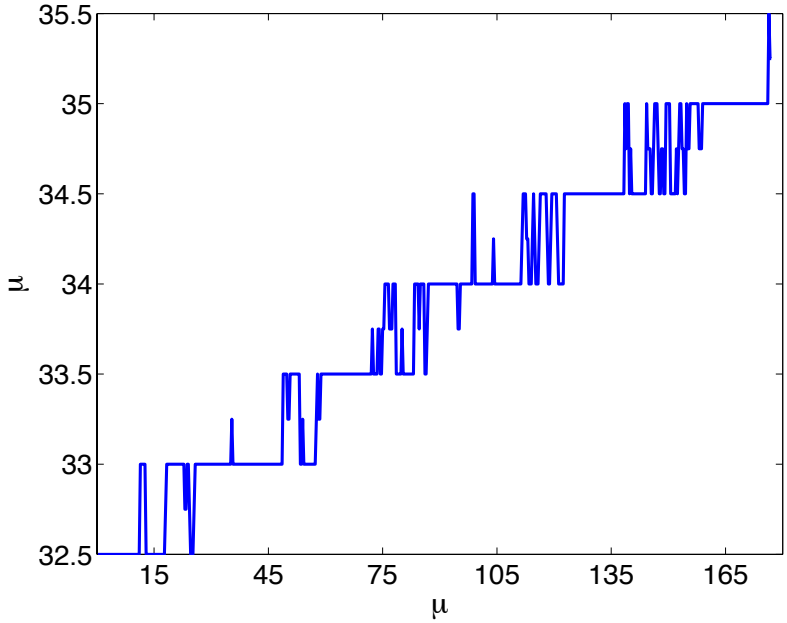

Figure 3.22: Sample A: calcite, 1-D data line

The increments in surface height is 0.5 μ. This is due to artifact of the discretization used in acquiring the microscope data. The width of each stair-step is around 31 μ. Figure 3.26 shows 2-D CWT coefficient calculated at wavelength of 32.2 μ, the value of the wavelength is consistent with the observation of the width of the stair-step pattern displayed in Figure 3.22. This 2-D CWT coefficient represents the surface component at this large wavelength, therefore we can not observe the details of the surface mineral since the surface is very smooth with the smallest roughness of 1.1774. At this large wavelength, the 2-D CWT coefficient proves to detect the surface objects with similar size, that is stair-step pattern.

The 2-D CWT coefficient calculated at 3.2 μ which is ten times smaller than the width of the stair-step pattern in the Figure 3.24 shows the random distribution of small object on the surface of calcite. This distribution is somewhat hard to observe in the data (Figures 3.9). When the wavelength of the wavelet increase to about of

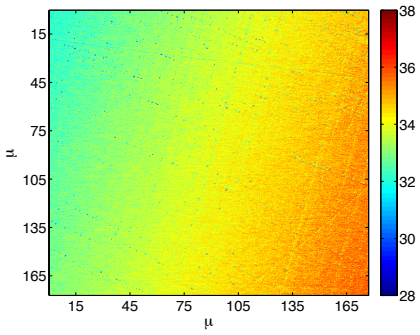

Figure 3.23: Sample A: calcite, with computed surface roughness parameter $R_s = 1.1774$

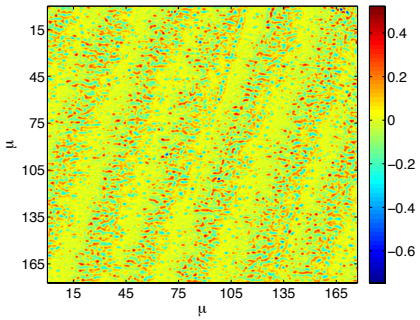

Figure 3.24: Sample A: calcite, 2-D CWT calculated at $\lambda = 3.2\ \mu$

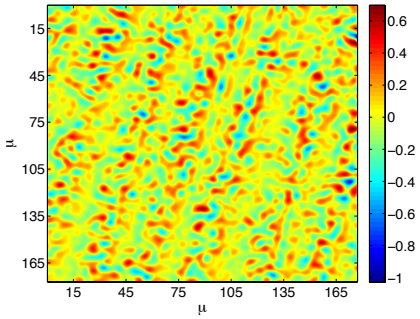

Figure 3.25: Sample A: calcite, 2-D CWT calculated at $\lambda = 9.6\ \mu$

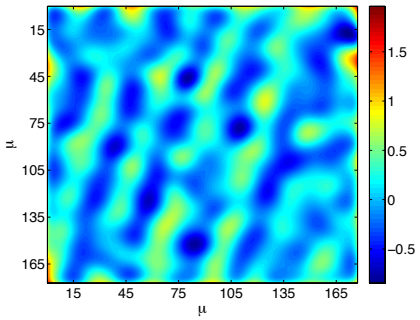

Figure 3.26: Sample A: calcite, 2-D CWT calculated at $\lambda = 32.2\ \mu$

9.6 μ, all the detail of the surface are lost, and the surface component is more rough, we can also observe the uniform distribution but with larger size objects. Since this sample is very smooth with $R_s = 1.1774$, in order to observe small object, one should calculate 2-D CWT coefficients with wavelength less than 3.2 μ. We do note that these points are artificial, since the apparent stair-step topography is simply an artifact of the limited resolution of the data set.

3.5.2.2 Sample B of calcite

Figure 3.10 shows another sample of calcite with almost the same size but with higher value of surface roughness of 1.2499, and we can observe the surface is more rough than the first sample (Figure 3.9). This sample is collected from an exposed mineral surface, and there is more effect of chemical and weathering reaction on the surface. The surface does not display any periodic pattern, but elevation gradually changes from the bottom of the sample, and there is high elevation object running from southwest to northeast on the surface. Figure 3.27 which displays the peak of 1-D vertical profile of the mineral surface data confirms further the existence of the high elevation object, which may be results from weathering process.

The 2-D CWT coefficient in Figure 3.31 calculated at wavelength of 34.6 μ reveals clearly the location of the high elevation object on the surface mineral. At this large wavelength we can observe the other large features displayed as blue and red with size of 34.6 μ. Figure 3.29 shows the 2-D CWT coefficient calculated at small wavelength of 4.1μ, we could not observe the previous high elevation object anymore, one can learn that the size of this object is much larger than 4.1 μ. From Figure 3.29, one can start to observe some few objects displayed as red with very high amplitude of 2 μ compared to the rest of the sample. These objects have very high surface energy therefore it is ready for chemical and weathering reactions These locations

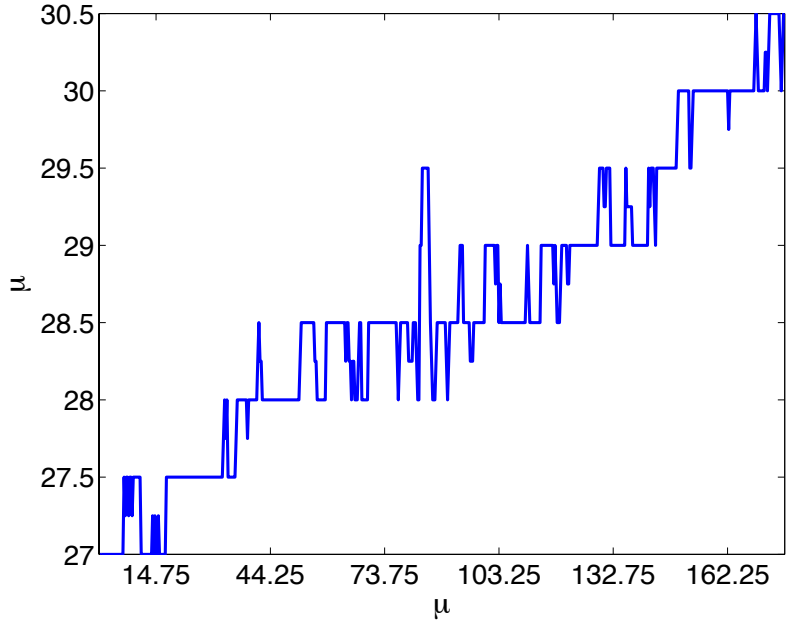

Figure 3.27: Sample B: calcite, with computed surface roughness parameter, 1-D data line

are more visible when 2-D CWT calculated at wavelength of 17.3 μ (Figure 3.30). The surface component is more rough but we lost the detail objects. We expect the erosion process geochemical reactions start from the above locations.

3.5.2.3 Sample C of calcite

The last sample of calcite is collected from exposed surface (Figure 3.11), the surface is very rough and it is very difficult to identify the location with high surface energy. The roughness of this sample is very high, which is 13.2589. The mineral surface may be the effects of very strong erosion of the geochemical and weathering processes. It is very difficult to determine the locations with high surface energy from the topographic (Figure 3.11). Since the surface is very rough, it is formed by small objects. Therefore we carry out 2-D CWT calculation with small wavelength of wavelet of 2.15 μ (Figure 3.33) and 4.3 μ (Figure 3.34). When we increase the

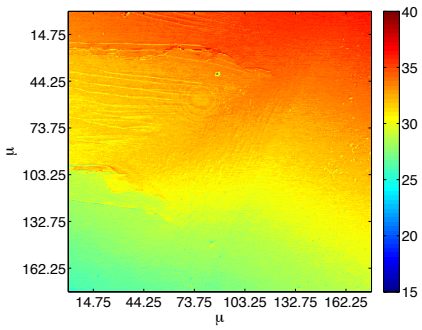

Figure 3.28: Sample B: calcite, with computed surface roughness parameter $R_s = 1.2499$

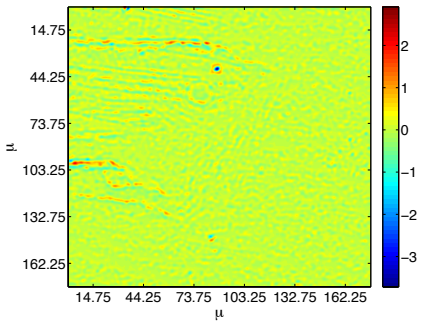

Figure 3.29: Sample B: calcite, 2-D CWT calculated at $\lambda = 4.1\ \mu$

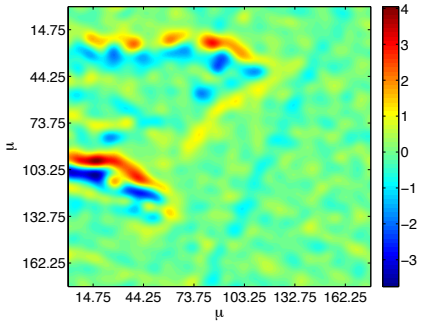

Figure 3.30: Sample B: calcite, 2-D CWT calculated at $\lambda = 17.3\ \mu$

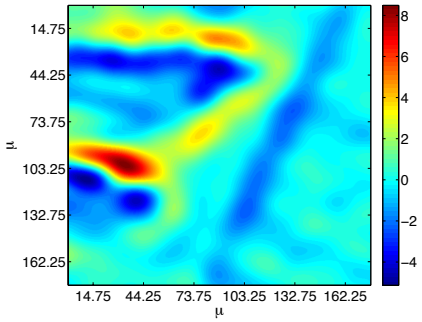

Figure 3.31: Sample B: calcite, 2-D CWT calculated at $\lambda = 34.6\ \mu$

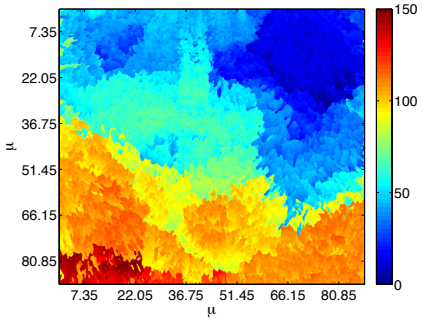

Figure 3.32: Sample C: calcite, with computed surface roughness parameter R_s = 13.2589

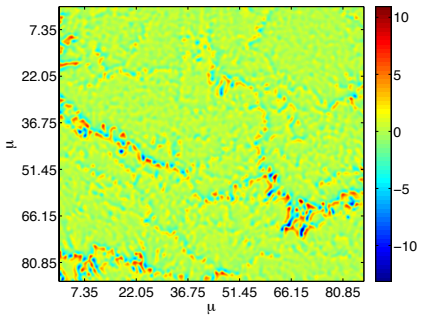

Figure 3.33: Sample C: calcite, 2-D CWT calculated at $\lambda = 2.15\ \mu$

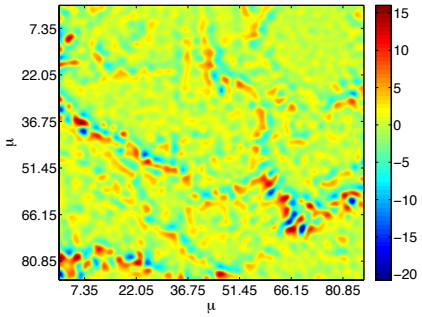

Figure 3.34: Sample C: calcite, 2-D CWT calculated at $\lambda = 4.3\ \mu$

wavelength from 2.15 μ and 4.3 μ, the surface component associated with the 2-D CWT coefficients become more rough, it also increases the maximum value of amplitude from 12 μ to 22 μ. Comparing to the topographic of the mineral in Figure 3.11, one now can identify the locations of the small objects with the size of 2.15 μ. These object have very high amplitude of around 10 while the rest of object on surface component have very small amplitudes. The location of these object therefore have very high surface energy which is critical for geochemical and weathering reactions.

3.6 Discussion

Equation 3.2 has been proposed as a statistic for measuring surface roughness and comparing measurements from different materials. However, results for the mineral samples we consider show the limited utility of this parameter, since four of five samples have very similar values of R_s between 1 and 2. In particular, the rough, weathered surface of Fe_2O_3 sample A was measured with a relatively coarse spacing of 2.485 microns. The similar sample B was measured with 0.159 microns. Thus, even though the mineral surfaces are very similar, the roughness statistic R_s for sample B is 2.8 compared to the sample A value of 1.21. This is because the finer sampling allows the measurement of more detailed variations in topography and thus the area ratio in equation 3.2 is larger. This is also why the computed R_s for the iron oxide sample A is essentially the same as that for the cleavage plane measured for calcite A (1.18). Thus R_s has clear limitations in its ability to characterize topography, and in the fact that it is a global measurement that provides no insights into spatial variations in roughness.

In contrast, the CWT coefficient maps for both data sets from the Fe_2O_3 (Figures 3.7 and 3.8) clearly identify the portions of the mineral roughness with the increased roughness at different spatial scales. Figure 3.13 shows that the surface, which has

clear structure in the original plot of its topography, has concentrated areas with sharper variations in height in the upper half of the image when measured at a wavelength of 24.5 μ. Even increased wavelengths of 73.6 and 122.7 μ show the same regions as having more structure in the upper portion of the image (Figures 3.14, 3.15). Only at the largest wavelength, 368.1 μ, does significant amplitude appear in wavelet coefficients in the bottom portion of the image (Figure 3.16). Thus the variation in elevation there is only present at comparatively long wavelengths, and the surface is rather smooth. Though the CWT approach does not directly yield a single number intended to represent roughness, it does make it easier to identify the specific locations with greatest contrast in height (roughness), especially when using the smallest wavelength, which also provides the best spatial resolution. This is important for geochemical studies, since these will be the locations where reactions will take place most rapidly.

The calcite B also presents an interesting example, since it is very smooth (Figure 3.27). While the original image shows very little variation, the CWT analysis identifies clear structure in the surface, in this case most obviously at the wavelength 17.4 μ (Figure 3.30). The more intense red and blue colors in this coefficient image again highlight portions of the mineral surface that have the largest variation in elevation, and thus will experience faster reactions. It is also interesting to note that the longest wavelength tested, 34.6 μ, also shows clearly a roughly linear surface feature that extends diagonally across the surface (Figure 3.31).

Calcite C is clearly the roughest mineral surface sampled in our data set, with the R_s value of 13.3 (Figure 3.11). In this case, the R_s value is useful in giving an indication of the variability in surface height. However, even when examining the surface data as shown in the figure, it is difficult to determine the areas with the greatest degree of roughness where we would expect reactions to be concentrated.

Here the wavelet results are also very useful, because the transform coefficients show several regions of greater amplitude at relatively small wavelengths of 2.15 and 4.3 μ (Figures 3.33, 3.34).

Future research could test these interpretations and analysis by conducting laboratory experiments where the measured mineral surfaces are subjected to chemical reactions. Repeating the surface topography measurements and CWT analyses after the reactions have taken place should show changes in the positions of rough edges. For example, the positions of the bands of red and blue colors marking rapid changes in heigh, edges, in Figure 3.34 should be found in different locations. Comparisons of such images could also then be used to infer how much of the mineral surface has been altered or removed during these geochemical experiments.

3.7 Conclusions

For the first time, 2-D CWT has been applied to study the surface roughness at very small scale (micron) such as surface of the minerals. The main purpose of this research topic is to characterize the surface roughness of mineral samples to reveal the structure pattern as well as the interested objects of the exposed surface to help understand the geochemical and weathering processes.

We collect two different types of mineral surfaces, one fresh crystal mineral surface of calcite and four exposed surface for two samples of Fe_2O_3 and two samples of calcite. For the un-exposed surface of calcite, the width of the stair-step pattern of the fresh-cut calcite have been detected by using 2-D CWT with wavelength of 32.2 μ. The other two surface samples of calcite and two samples of Fe_2O_3 show the erosion effects, the application of 2-D CWT analysis help to localize any objects with any size created by geochemical and weathering reactions by carrying out 2-D CWT coefficient at corresponding wavelength. This property help us to understand better

the characterization of surface roughness during the geochemical and weathering processes. The 2-D CWT coefficients also help us to localize the positions on the mineral surface with high surface energy. the geochemical and weathering reactions occur initially on these locations. In the future works, if we can carry out the 2-D CWT inversion, we can rebuild the topographic map of the mineral at certain wavelength of the wavelet, then calculate the surface roughness by using equation 3.2. We can see direct the relationship between the surface roughness and the wavelength.

4. CONCLUSIONS

Ins this section, I summarize the scientific contributions of the application of 2-D CWT to study the marine seismic data and mineral surface data.

In this dissertation, we propose the application of 2-D CWT to characterize the basement of oceanic plateaus such as Tamu Massif of Shatsky Rise. We use the 2-D normalized anisotropic Mexican hat wavelet to make quantitative comparisons of results with different frequency and wavenumber. We find that it is important that we apply correct normalization constants in the equation 2.8, to allow quantitative comparisons of coefficients for different wavelengths and frequencies. The results of the 2-D CWT analysis on recent marine seismic data acquired over Tamu Massif of Shatsky Rise help better reveal the structure and lateral variation of the basement. All of the images from 2-D CWT show that the amplitude of incoherent noise is reduced in comparison to that of laterally continuous events. We also show the comparison between the conventional bandpass filtering and 2-D CWT. The results show that in some cases conventional bandpass filtering may be adequate for facilitating interpretation of images, the CWT will be a good option when the enhancement of lateral continuity and minimization of signal with low coherence is required. The test applications also show that is important to review CWT results with different combinations of frequency and wavelength to select optimal values. In several cases, the CWT provides benefits for interpretation by varying the horizontal wavelength parameter to better correlate lateral reflectors which are associated as intra-basement reflectors. On one line, the 2-D CWT allowed detection of possible faults not observed in the original image, and in another example new dome-like features suggesting lava intrusions were detected in the CWT image. These exam-

ples help support the role of this approach in interpreting seismic images acquired in areas such as the Shatsky Rise. In the future works, in order to understand better deeper part of Tamu Massif oceanic crust, one should complete more sets of marine seismic data so we will have a complete the interpretation of the oceanic crust. It is very crucial to understanding the volcanism evolution.

For the first time, 2-D CWT has been applied to study the surface roughness at very small scale (micron) such as surface of the minerals. The main purpose of this research topic is to characterize the surface roughness of mineral samples to reveal the structure pattern as well as the interested objects of the exposed surface to help understand the geochemical and weathering processes.

We collect two different types of mineral surfaces, one fresh crystal mineral surface of Calcite and four exposed surface for two samples of Fe_2O_3 and two samples of Calcite minerals. For the un-exposed surface of Calcite mineral, the width of the stair-step pattern of the fresh-cut Calcite mineral have been detected by using 2-D CWT with wavelength of 32.2 μ. The other two surface samples of Calcite and two samples of Fe_2O_3 show the erosion effects, the application of 2-D CWT analysis help to localize any objects with any size created by geochemical and weathering reactions by carrying out 2-D CWT coefficient at corresponding wavelength. This property help us to understand better the characterization of surface roughness during the geochemical and weathering processes. The 2-D CWT coefficients also help us to localize the positions on the mineral surface with high surface energy. the geochemical and weathering reactions occur initially on these locations. In the future works, if we can carry out the 2-D CWT inversion, we can rebuild the topographic map of the mineral at certain wavelength of the wavelet, then calculate the surface roughness by using equation 3.2. We can see direct the relationship between the surface roughness and the wavelength.

REFERENCES

Addison, P. S., 2002, The illustrated wavelet transform handbook: Institute of Physics, London, UK.

Allen, J. B., 1977, Short time spectral analysis, synthesis, and modification by discrete fourier transform: IEEE Transactions on Acoustic, Speech, Signal Processing, **25**, 235–238.

Allmann, B. P., 2008, Earthquake rupture imaging and multiscale stress drop estimation: Master's thesis, University of California, San Diego.

Anderson, D. L., Tanimoto, T., and Zhang, Y.-S., 1992, Plate tectonics and hotspots: The third dimension: Science, **256**, 1645–1651.

Antoine, J.-P., Vandergheynst, P., and Ali, S. T., 2004, Two-dimensional wavelets and their relatives: Cambridge University Press, Cambridge, UK.

Becker, U., Rosso, K. M., and Hochella, M., 2001, The proximity effect on semiconducting mineral surfaces: a new aspect of mineral surface reactivity and surface complexation theory?: Geochimica et Cosmochimica Acta, **65**, no. 16, 2641 – 2649.

Booth, A. M., Roering, J. J., and Perron, J. T., 2009, Automated landslide mapping using spectral analysis and high-resolution topographic data: Puget sound lowlands, Washington, and Portland Hills, Oregon: Geomorphology, **109**, no. 34, 132–147.

Bralower, T. J., Silva, I. P., and Malone, M. J., 2006, 1. Leg 198 Synthesis: A Remarkable 120-m.y. Record of Climate and Oceanography from Shatsky Rise, Northwest Pacific Ocean:, volume 198 ODP Scientific Results, College Station, TX.

Coffin, M. F., and Eldholm, O., 1994, Large igneous province: Crustal structure, dimensions, and external consequences: Reviews of Geophysics, **32**, no. 1, 1–36.

Darrozes, J., Gaillot, P., de Saint Blanquat, M., and Bouchez, J. L., 1997, Software for multi-scale image analysis: The normalized optimized anisotropic wavelet coefficient method: Computers and Geosciences, **23**, no. 8, 889–895.

Daubechies, I., 1992, Ten lectures on wavelets: SIAM, Philadelphia.

Foufoula-Georgiou, E., and Kumar, P., 1994, Wavelets in geophysics: Academic Press, San Diego, California.

Foulger, G. R., 2007, The "plate" model for the genesis of melting anomalies: The Geological Society of America Special Paper, **430**, 1–28.

Frantziskonis, G. N., Simon, L. B., Woo, J., and Matikas, T. E., 2000, Multiscale characterization of pitting corrosion and application to an aluminum alloy: Eur. J. Mech. A/Solids, **19**, no. 2, 309–318.

Gaillot, P., Darrozes, J., de Saint Blanquat, M., and Ouillon, G., 1997, The normalised optimised anisotropic wavelet coefficient (NOAWC) method: An image processing tool for multiscale analysis of rock fabric: Geophysical Research Letters, **24**, no. 14, 1819–1822.

Gersztenkorn, A., 2012, A new approach for detecting topographic and geologic information in seismic data: Geophysics, **77**, 81–90.

Goloshubin, G., Korneev, V., Daley, T., and Silin, D., 2004, Seismic low-frequency effects from fluid-saturated reservoir: Geophysics, **69**, no. 2, 522 – 532.

Gradstein, F. M., Ogg, J. G., and Smith, A. G., 2004, A geologic time scale: Cambridge University Press, Cambridge, UK.

Houtz, R. E., and Ludwig, W. J., 1979, Distribution of reverberant subbottom layers in the southwest pacific basin: Journal of Geophysical Research, **84**, no. B7, 3497.

Josso, B., 2002, Frequency normalised wavelet transform for surface roughness analysis and characterization: Wear, **252**, 491–500.

Kazemeini, S. H., Juhlin, C., Zinck-Jørgensen, K., and Norden, B., 2008, Application of the continuous wavelet transform on seismic data for mapping of channel deposits and gas detection at the CO2SINK site, Ketzin, Germany: Geophysical Prospecting, **57**, 111–123.

Klaus, A., and Sager, W. W., Eds. Data report: High-resolution site survey seismic reflection data for ODP Leg 198 drilling on Shatsky Rise, Northwest Pacific, volume 198. Proceedings of the Ocean Drilling Program, 2002.

Korenaga, J., and Sager, W. W., 2012, Seismic tomography of Shatsky Rise by adaptive importance sampling: Journal of Geophysical Research, **117**, 1 – 24.

Korneev, G., Goloshubin, V., and Vingalov, V., 2002, Seismic low-frequency effects from oil-saturated reservoir zones: 72th Annual International Meeting, SEG, Expanded Abstracts, **72**, 1813 – 1816.

Lange, D. A., Jennings, H. M., and Shah, S. P., 1993, Analysis of surface roughness using confocal microscopy: Journal of Materials Science, **28**, 3879–3884.

Ludwig, W. J., and Houtz, R. E., 1979, Isopach map of sediments in the Pacific Ocean basin and marginal sea basins: American Association of Petroleum Geologists, Tulsa, Oklahoma.

Mahoney, J. J., and Spencer, K. J., 1991, Isotopic evidence for the origin of the Manihiki and Ontong Java oceanic plateaus: Earth and Planery Science Letters, **104**, 196–210.

Mahoney, J., Duncan, R., Tejada, M., Sager, W., and Bralower, T., 2005, Jurassic-Cretaceous boundary age and mid-ocean-ridge type mantle source for Shatsky Rise: Geology, **33**, 185–188.

Mezghania, S., 2011, Multiscale characterizations of painted surface appearance by continuous wavelet transform: Journal of Materials Processing Technology, **211**, 205–211.

Miao, X.-G., and Moon, W. M., 1999, Application of wavelet transform in reflection seismic data analysis: Geosciences Journal, **3**, no. 3, 171 – 179.

Moktadir, Z., and Sato, K., 2000, Wavelet characterization of the submicron surface roughness of anisotropically etched silicon: Surface Science, **470**, 57–62.

Morlet, J., Arens, G., Fourgeau, E., and Giard, D., 1982, Wave propagation and sampling theory - Part II: Sampling theory and complex waves: Geophysics, **47**, no. 2, 222–236.

Nakanishi, M., Sager, W. W., and Klaus, A., 1999, Magnetic lineations within Shatsky Rise, northwest Pacific Ocean: Implications for hot spot-triple junction interaction and oceanic plateau formation: Journal of Geophysical Research, **104**, no. B4, 7539–7556.

Namba, Y., Yu, J., Bennett, J. M., and Yamashita, K., 2000, Modeling and Measurements of Atomic Surface Roughness: Applied Optics, **39**, 2705–2718.

Neupauer, R. M., and Powell, K. L., 2005, A fully-anisotropic Morlet wavelet to identify dominant orientations in a porous medium: Computers and Geosciences, **31**, 465–471.

Nyander, A., Addison, P. S., McEwan, I., and Pender, G., 2003, Analysis of river bed surface roughnesses using 2D wavelet transform-based methods: Arabian Journal

for Science and Engineering, **28**, 107–121.

Poppeliers, C., 2011, Multiwavelet seismic wave gradiometry: Bulletin of the Seismological Society of America, **101**, 2108–2121.

Reed, T. R., and Dubuf, J. M. H., 1993, A review of recent texture segmentation and feature extraction techniques: CVGIP: Image Understanding, **57**, no. 3, 359 – 372.

Richards, M. A., Duncan, R. A., and Courtillot, V. E., 1989, Flood basalts and hot-spot tracks: Plume heads and tails: Science, **246**, 103–107.

Sager, W., and Han, H.-C., 1993, Rapid formation of the Shatsky Rise oceanic plateau inferred from its magnetic anomaly: Nature, **364**, 610–613.

Sager, W. W., Kim, J., Klaus, A., Nakanishi, M., and Khankishieva, L. M., 1999, Bathymetry of Shatsky Rise, northwest Pacific Ocean: Implications for ocean plateau development at a triple junction: Journal of Geophysical Research, **104**, no. B4, 7557–7576.

Sager, W. W., Sano, T., and Geldmacher, J., 2010, Proceedings of the integrated ocean drilling program: Integrated Ocean Drilling Program Management International, Tokyo, Japan, **324**.

Sager, W. W., Sano, T., and Geldmacher, J., 2011, IODP Expedition 324: Ocean drilling at Shatsky Rise gives clues about oceanic plateau formation: Scientific Drilling, **12**, 24–31.

Sager, W. W., Sano, T., and Geldmacher, J., 2012, How do oceanic plateaus form? Clues from drilling Shatsky Rise: EOS, Transactions American Geophysical Union, **92**, 37 – 38.

Sager, W. W., Zhang, J., Korenaga, J., Sano, T., Koppers, A. A., Widdowson, M.,

and Mahoney, J. J., 2013, An immense shield volcano within the Shatsky Rise oceanic plateau, northwest Pacific Ocean: Nature Geoscience, **6**, 976 – 981.

Sager, W. W., 2005, What built Shatsky Rise, a mantle plume or ridge tectonics?: Geological Society of America Special Papers, **388**, 721–733.

Sahimi, M., and Hashemi, M., 2001, Wavelet identification of the spatial distribution of fractures: Geophysical Research Letters, **28**, 611–614.

Sano, T., Shimizu, K., Ishikawa, A., Senda, R., Chang, Q., Kimura, J.-I., Widdowson, M., and Sager, W. W., August 2012, Variety and origin of magmas on Shatsky Rise, Northwest Pacific Ocean: Geochemistry Geophysics Geosystems, **13**, no. 8, 1–25.

Saunders, A. D., 2005, Large Igneous Provinces: Origin and Environmental Consequences: Elements, **1**, 259–263.

Shipboard Scientific Party, 2002, Leg 198 summary:, volume 192 Proceedings of the Ocean Drilling Program, Initial Report, College Station, TX, doi:10.2973/odp.proc.ir.198.101.2002 edition.

Sinha, S., Routh, P. S., Anno, P. D., and Castagna, J. P., 2005, Spectral decomposition of seismic data with continuous-wavelet transform: Geophysics, **70**, no. 6, 19–25.

Sliter, W. V., and Brown, G. R., 1993, Shatsky Rise: seismic stratigraphy and sedimentary record of Pacific paleoceanography since the Early Cretaceous: Proceedings of the Ocean Drilling Program, **132**, 3–13.

Smith, W. H. F., and Sandwell, D. T., 1997, Global sea floor topography from satellite altimetry and ship depth soundings: Science, **277**, no. 5334, 1956–1962.

Smith, M., Perry, G., Stein, J., Bertrand, A., and Yu, G., 2008, Extending seismic

bandwidth using the continuous wavelet transform: Leveraging Technology, **26**, 97 – 102.

Stout, K., 1993, Development of Methods for Characterisation of Roughness in Three Dimensions: Commission of the European Communities, University of Birmingham Edgbaston, Birmingham, UK.

Sun, J. P., Castagna, S., and Siegfried, R. W., 2003, Instantaneous spectral analysis: Detection of low-frequency shadows associated with hydrocarbons: The Leading Edge, **22**, no. 2, 120–127.

Thomas, H., Nobuhiro, I., and John, W., 1976, Mesozoic sea-floor spreading in the North Pacific: Geophysical Monograph Series, **19**, 205–226.

Thomas, T. R., 1982, Rough surfaces: Longman, London, UK.

Torrence, C., and Compo, G. P., 1998, A Practical Guide to Wavelet Analysis: Bulletin of the American Meteorological Society, **79**, 61–78.

Tuceryan, M., and Jain, A. K., 1998, Texture analysis, *in* Chen, C. H., and Pau, L. F., Eds., The Handbook of Pattern Recognition and Computer Vision (2nd Edition): World Scientific Publishing Co., Singapore, 207 – 248.

White, A. F., and Brantley, S. L., 2003, The effect of time on the weathering of silicate minerals: why do weathering rates differ in the laboratory and field?: Chemical Geology, **202**, no. 34, 479 – 506.

Whitehouse, D. J., 1994, Handbook of surface metrology: The Institute of Physics, London, UK.

Zahouani, H., Mezghani, S., Vargiolu, R., and Dursapt, M., 2008, Identification of manufacturing signature by 2D wavelet decomposition: Wear, **264**, no. 56, 480 – 485.

Zhang, J., Sager, W., and Korenaga, J., 2013, Shatsky Rise Oceanic Plateau from 2D Multi-channel Seismic Reflection Profiles and Implications for Oceanic Plateau Formation: Special Papers of Geological Society of America, in press.